

# Gravitational effects on Faraday instability in a viscoelastic liquid

I.B. Ignatius<sup>1</sup> , B. Dinesh<sup>2</sup> , G.F. Dietze<sup>3</sup> and R. Narayanan<sup>1</sup>

<sup>1</sup>Department of Chemical Engineering, University of Florida, Gainesville, FL 32611, USA

<sup>2</sup>Department of Chemical Engineering and Technology, Indian Institute of Technology (BHU) Varanasi, Varanasi, UP 221005, India

<sup>3</sup>FAST, CNRS, Université Paris-Saclay, Orsay 91405, France

**Corresponding author:** I.B. Ignatius, [iginbenny@gmail.com](mailto:iginbenny@gmail.com)

(Received 5 August 2024; revised 20 March 2025; accepted 21 March 2025)

The influence of parametric forcing on a viscoelastic fluid layer, in both gravitationally stable and unstable configurations, is investigated via linear stability analysis. When such a layer is vertically oscillated beyond a threshold amplitude, large interface deflections are caused by Faraday instability. Viscosity and elasticity affect the damping rate of momentary disturbances with arbitrary wavelength, thereby altering the threshold and temporal response of this instability. In gravitationally stable configurations, calculations show that increased elasticity can either stabilize or destabilize the viscoelastic system. In weakly elastic liquids, higher elasticity increases damping, raising the threshold for Faraday instability, whereas the opposite is observed in strongly elastic liquids. While oscillatory instability occurs in Newtonian fluids for all gravity levels, we find that parametric forcing below a critical frequency will cause a monotonic instability for viscoelastic systems at microgravity. Importantly, in gravitationally unstable configurations, parametric forcing above this frequency stabilizes viscoelastic fluids, until the occurrence of a second critical frequency. This result contrasts with the case of Newtonian liquids, where under the same conditions, forcing stabilizes a system for all frequencies below a single critical frequency. Analytical expressions are obtained under the assumption of long wavelength disturbances predicting the damping rate of momentary disturbances as well as the range of parameters that lead to a monotonic response under parametric forcing.

**Key words:** faraday waves, thin films, viscoelasticity

## 1. Introduction

The damping rate of the interface of a viscoelastic liquid, such as a polymeric solution, depends on both its viscous and elastic properties, when the fluid is subjected to momentary disturbances. The viscous component dissipates the imposed disturbances, while the elastic component gives rise to restorative forces due to elastic stresses. The memory associated with these stresses therefore alters the behaviour of the fluid when it is subjected to time-periodic acceleration, which is the subject of the current study.

The influence of viscoelasticity is apparent in its notable impact on the instability threshold that arises from parametric forcing, as reported in early theoretical studies (Kumar 1999; Müller & Zimmermann 1999). These theoretical investigations compared the resonant characteristics of Newtonian fluids with polymeric solutions in the presence of gravity. The onset of the instability, known as Faraday instability, was predicted by a mathematical model similar to the one proposed by Kumar & Tuckerman (1994), upon incorporating a Maxwell constitutive relationship (Bird *et al.* 1987). The mechanical analogue of the dynamic behaviour of Maxwell fluids is often represented by a dashpot and spring in series, where the dashpot reflects the viscous response to disturbances and the spring reflects the elastic response (Guyon *et al.* 2015). Viscoelastic fluids, such as the one studied by Kumar (1999) and Müller & Zimmermann (1999), following a Maxwell constitutive relationship, behave more like a viscous liquid under low-frequency oscillatory disturbances and more like an elastic solid under high-frequency oscillatory disturbances. By contrast, soft polymeric gels characterized by Kelvin–Voigt constitutive laws exhibit the opposite response (Morozov & Spagnolie 2015). Likewise, different dynamic behaviour and temporal response are reported when solid gels are subjected to parametric forcing as seen in several interesting studies (Shao *et al.* 2018, 2020; Bevilacqua *et al.* 2020).

Focusing on the dynamical behaviour of a Maxwell fluid in the presence of parametric forcing, linear stability calculations were performed by Kumar (1999) and Müller & Zimmermann (1999) who assumed the properties of various polymer solutions with different levels of elasticity, expressed in terms of the relaxation time, i.e. the time scale for the polymer chains to relax within the solvent. It was demonstrated that the threshold amplitude for the onset of Faraday instability decreases with an increase in elasticity. The findings of these studies, which assumed infinitely wide and deep fluid layers, revealed a predominantly harmonic interface response for frequency ranges where the forcing frequency is close to the inverse of the relaxation time. Beyond these frequency ranges, it was shown that a subharmonic mode becomes more unstable than the harmonic mode. This is in contrast to a Newtonian liquid, where a subharmonic response is always dominant in deep liquid layers (Kumar 1996). In the work of Kumar (1999), Faraday forcing in finite depths were also considered and it was observed that the harmonic mode becomes more dominant than the case of infinitely deep liquids. This result was attributed to increased vertical viscous stresses.

Experimental validation of these theories was provided by Wagner *et al.* (1999) who used a dilute solution of polyacrylamide-co-acrylic acid polymer in a glycerol–water mixture solvent. Such a fluid mixture is not shear-thinning and follows a Maxwell constitutive relation. Through these experiments, the authors not only confirmed the presence of harmonic patterns but also demonstrated that the theoretical models of Müller & Zimmermann (1999) and Kumar (1999) accurately predict the experimental onset of Faraday waves. By contrast, experiments performed by Raynal *et al.* (1999), Ballesta & Manneville (2005) and Cabeza & Rosen (2007) employing shear-thinning polymeric

solutions, while showing qualitative agreement, revealed quantitative discrepancies with the theories for non-shear-thinning fluids (Kumar 1999; Müller & Zimmermann 1999).

In a recent study, Schön & Bestehorn (2023) investigated the threshold limits and nonlinear behaviour of the interface of a Maxwell fluid undergoing resonant instability. They used a reduced-order model, making a thin-layer approximation that included both inertial and elastic terms, crucial to predicting the Faraday instability. Using this model, they observed that the threshold amplitude for the onset of Faraday instability decreases with an increase in frequency and does so at a faster rate compared with a Newtonian liquid.

The principal purpose of the current work is to study the effect of different gravity levels on the parametric forcing of a layer of viscoelastic fluid. To this end, we consider the same constitutive model, i.e. the Maxwell model, studied theoretically by Kumar (1999), Müller & Zimmermann (1999), Schön & Bestehorn (2023) and experimentally by Wagner *et al.* (1999), now focusing on the effect of gravity on a parametrically forced viscoelastic fluid layer.

The current work differs from earlier studies on gravitationally stable configurations in two significant ways. First, we present new findings for the gravitationally stable case in the weakly elastic limit. Second, we examine two additional scenarios: one in which gravity is weak, i.e. the microgravity case and another where the system becomes gravitationally unstable. As a result, we make several important observations. In the gravitationally stable case, while Kumar (1999) observed that the threshold for Faraday instability decreases as the Deborah number increases for high Deborah values under Earth's gravity, our study goes further by exploring weakly elastic fluids, i.e. having small relaxation times. Upon doing so, we find that in the weakly elastic limit, the threshold for Faraday instability actually increases with elasticity, which contrasts with the behaviour observed in strongly elastic fluids. These results are supported by asymptotic expressions for the inverse time constants in the long-wavelength limit. In the microgravity case, we observe a striking transition from oscillatory to monotonic behaviour as the gravity level decreases. As gravity approaches zero, monotonic instability dominates, a phenomenon that has not been previously reported. This shift to monotonic instability in microgravity has implications for the case in which the fluid is gravitationally unstable. Finally, in the gravitationally unstable case, unlike the case of Newtonian fluids where parametric forcing always has a stabilizing effect (Serman-Cohen *et al.* 2017), the present study reveals the possibility of either stabilization or destabilization for the case of viscoelastic fluids. Specifically, upon considering fluids of finite lateral extent, we find a range of forcing amplitudes between two critical parametric frequencies where we can stabilize an otherwise gravitationally unstable system, without triggering resonance. This stands in stark contrast to a Newtonian fluid system where we have only one critical frequency below which complete stabilization may be achieved (Ignatius *et al.* 2024). These new results are supported by algebraic expressions derived from a low-dimensional model based on a long-wavelength approximation (Ruyer-Quil & Manneville 2000). These expressions not only predict the instability ranges but also provide insight into the physical phenomena involved in the parametric forcing of viscoelastic fluids.

The manuscript is arranged as follows. In § 2, we give the mathematical model for the parametric forcing of a Maxwell liquid in a configuration as described in figure 1. In § 3, we investigate the effect of elasticity on the fluid's damping rates, or more generally the inverse time constants, to momentary disturbances. The behaviour of the inverse time constants with fluid elasticity forecasts the effect of the latter on the threshold amplitude of Faraday instability as well as the interface's temporal response in both gravitationally

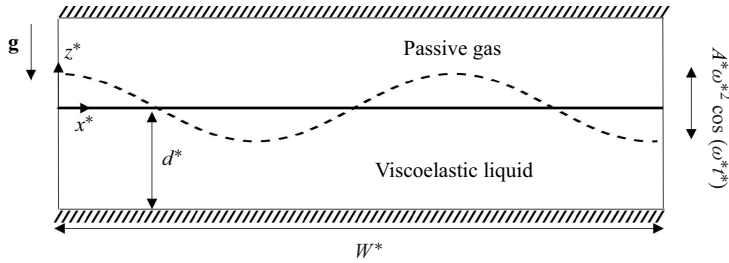


Figure 1. Schematic of the studied configuration in the moving frame of reference. Depicted is a viscoelastic liquid layer in contact with a passive gas aligned with the gravity vector,  $\mathbf{g}$ . The fluid container is subject to a vertical mechanical acceleration,  $A^*\omega^{*2}\cos(\omega^*t^*)\mathbf{e}_z$ , with respect to the laboratory frame.

stable and microgravity configurations. This is analysed in § 4. Finally, in § 5, we discuss the influence of parametric forcing on a gravitationally unstable viscoelastic system.

## 2. Mathematical model

Consider a viscoelastic liquid layer of unperturbed height,  $d^*$ , in a container of width,  $W^*$ , and in contact with a passive gas as shown in figure 1. The fluid system is subjected to the gravitational acceleration,  $\mathbf{g}$ , and a mechanical oscillation of angular frequency,  $\omega^*$ , and amplitude,  $A^*$ , in the direction of gravity. We consider this system in the moving frame of reference,  $x^*, z^*$ , i.e. a frame that rests on the initial flat interface and moving with the container. In addition to properties such as density,  $\rho$ , viscosity,  $\mu$ , and surface tension,  $\gamma$ , the liquid possesses a shear modulus,  $G$ , which imparts elastic character. Fluid flow in the system is governed by the nonlinear equations of momentum subject to continuity and appropriate interfacial conditions. These are expressed next in the moving frame of reference first in unscaled form, and then rendered dimensionless using suitable scaling variables.

### 2.1. Nonlinear equations

The continuity and momentum equations are

$$\nabla^* \cdot \mathbf{v}^* = 0 \quad (2.1)$$

and

$$\rho \left( \frac{\partial \mathbf{v}^*}{\partial t^*} + \mathbf{v}^* \cdot \nabla^* \mathbf{v}^* \right) = -\nabla^* p^* + \nabla^* \cdot \boldsymbol{\tau}^* - \rho \left( g + A^*\omega^{*2}\cos(\omega^*t^*) \right) \mathbf{e}_z, \quad (2.2)$$

where  $\boldsymbol{\tau}^*$  is the stress tensor and  $\mathbf{e}_z$  is the unit vector in the  $z$ -direction. The constitutive equation for the viscoelastic liquid is described by an upper-convected Maxwell equation (Morozov & Spagnolie 2015), a nonlinear model that includes frame-invariant derivatives in the stress-strain rate relationship. This is expressed as

$$\boldsymbol{\tau}^* + \lambda \left( \frac{\partial \boldsymbol{\tau}^*}{\partial t^*} + \mathbf{v}^* \cdot \nabla^* \boldsymbol{\tau}^* - (\nabla^* \mathbf{v}^*)^T \cdot \boldsymbol{\tau}^* - \boldsymbol{\tau}^* \cdot (\nabla^* \mathbf{v}^*) \right) = \mu \left( \nabla^* \mathbf{v}^* + (\nabla^* \mathbf{v}^*)^T \right), \quad (2.3)$$

where  $\lambda = \mu/G$  is the relaxation time.

At the bottom wall,  $z^* = -d^*$ , we impose no-slip and no-penetration conditions, i.e.

$$\mathbf{v}^* = \mathbf{0}. \quad (2.4)$$

At the impenetrable interface,  $z^* = h^*(\mathbf{x}^*, t^*)$ , the jump mass balance gives

$$(\mathbf{v}^* - \mathbf{u}^*) \cdot \mathbf{n}^* = 0. \quad (2.5)$$

The jump force balance yields an equation in terms of the stress tensor,  $\boldsymbol{\tau}^*$ , and is given by

$$-p^* \mathbf{n}^* + \mathbf{n}^* \cdot \boldsymbol{\tau}^* + \gamma \mathbf{n}^* \nabla^* \cdot \mathbf{n}^* = 0, \quad (2.6)$$

for which the interface speed,  $\mathbf{u}^* \cdot \mathbf{n}^*$ , and the unit normal,  $\mathbf{n}^*$ , are given by

$$\mathbf{u}^* \cdot \mathbf{n}^* = \frac{\frac{\partial h^*}{\partial t^*}}{\left(1 + \left(\frac{\partial h^*}{\partial x^*}\right)^2\right)^{\frac{1}{2}}} \text{ and } \mathbf{n}^* = \frac{-\frac{\partial h^*}{\partial x^*} \mathbf{e}_x + \mathbf{e}_z}{\left(1 + \left(\frac{\partial h^*}{\partial x^*}\right)^2\right)^{\frac{1}{2}}}. \quad (2.7)$$

The characteristic scales used to convert the governing equations into scaled form are

$$\begin{aligned} x &= \frac{x^*}{W^*}, \quad z = \frac{z^*}{d^*}, \quad t = \frac{t^*}{\left(\frac{d^*}{\epsilon U}\right)}, \quad \omega = \omega^* \left(\frac{d^*}{\epsilon U}\right), \quad u = \frac{u^*}{U}, \quad w = \frac{w^*}{\epsilon U}, \\ p &= \frac{p^*}{\left(\frac{\mu U}{d^*}\right)}, \quad \tau_{xx} = \frac{\tau_{xx}^*}{\left(\frac{\epsilon \mu U}{d^*}\right)}, \quad \tau_{xz} = \frac{\tau_{xz}^*}{\left(\frac{\mu U}{d^*}\right)} \text{ and } \tau_{zz} = \frac{\tau_{zz}^*}{\left(\frac{\epsilon \mu U}{d^*}\right)}, \end{aligned} \quad (2.8)$$

where  $U$  is a characteristic velocity in the  $x$ -direction to be defined in § 4, (4.1).

Note that we render  $x$  and  $z$  dimensionless using  $W^*$  and  $d^*$ , respectively. This leads to a length scale separation parameter,  $\epsilon$ , given by  $\epsilon = d^*/W^*$ , which will play an important role when we consider the long-wave limit of the problem to derive algebraic formulae that can predict stability ranges. Non-dimensionalizing equations (2.1) and (2.2) and expressing them in component form, we get

$$\frac{\partial u}{\partial x} + \frac{\partial w}{\partial z} = 0, \quad (2.9)$$

$$\epsilon Re \left( \frac{\partial u}{\partial t} + u \frac{\partial u}{\partial x} + w \frac{\partial u}{\partial z} \right) = -\epsilon \frac{\partial p}{\partial x} + \epsilon^2 \frac{\partial \tau_{xx}}{\partial x} + \frac{\partial \tau_{xz}}{\partial z} \quad (2.10a)$$

and

$$\epsilon^3 Re \left( \frac{\partial w}{\partial t} + u \frac{\partial w}{\partial x} + w \frac{\partial w}{\partial z} \right) = -\epsilon \frac{\partial p}{\partial z} + \epsilon^2 \frac{\partial \tau_{xz}}{\partial x} + \epsilon^2 \frac{\partial \tau_{zz}}{\partial z} - \epsilon (\mathcal{G} + \mathcal{A} \cos(\omega t)). \quad (2.10b)$$

Likewise the scaling of (2.3) yields

$$\tau_{xx} + De \left[ \frac{\partial \tau_{xx}}{\partial t} + u \frac{\partial \tau_{xx}}{\partial x} + w \frac{\partial \tau_{xx}}{\partial z} - 2 \left( \tau_{xx} \frac{\partial u}{\partial x} + \frac{1}{\epsilon^2} \tau_{xz} \frac{\partial u}{\partial z} \right) \right] = 2 \frac{\partial u}{\partial x}, \quad (2.11a)$$

$$\tau_{xz} + De \left[ \frac{\partial \tau_{xz}}{\partial t} + u \frac{\partial \tau_{xz}}{\partial x} + w \frac{\partial \tau_{xz}}{\partial z} - \left( \epsilon^2 \tau_{xx} \frac{\partial w}{\partial x} + \tau_{zz} \frac{\partial u}{\partial z} \right) \right] = \frac{\partial u}{\partial z} + \epsilon^2 \frac{\partial w}{\partial x} \quad (2.11b)$$

and

$$\tau_{zz} + De \left[ \frac{\partial \tau_{zz}}{\partial t} + u \frac{\partial \tau_{zz}}{\partial x} + w \frac{\partial \tau_{zz}}{\partial z} - 2 \left( \tau_{xz} \frac{\partial w}{\partial x} + \tau_{zz} \frac{\partial w}{\partial z} \right) \right] = 2 \frac{\partial w}{\partial z}. \quad (2.11c)$$

In the above, the Reynolds number is given by  $Re = \rho U d^* / \mu$ . It is the ratio of the characteristic time due to viscous damping and the characteristic time due to flow. The Deborah number,  $De = \lambda(\epsilon U / d^*) = (\mu / G)(\epsilon U / d^*)$  characterizes the ratio of the relaxation time due to elasticity and the characteristic time due to flow. The ratio  $De / Re$  is thus independent of the characteristic flow speed,  $U$ . The scaled gravity is given by  $G = \rho g d^{*2} / (\mu U)$  and scaled forcing amplitude becomes  $\mathcal{A} = \rho A^* \omega^{*2} d^{*2} / (\mu U)$ .

The scaled boundary conditions are

$$u = 0 \text{ and } w = 0 \text{ at } z = -1, \quad (2.12)$$

while at the interface,  $z = h(x, t)$ , the jump mass balance condition become

$$\epsilon w - \epsilon u \frac{\partial h}{\partial x} = \epsilon \frac{\partial h}{\partial t}, \quad (2.13a)$$

and the tangential and normal components of the force balance become

$$\tau_{xz} \left( 1 - \epsilon^2 \left( \frac{\partial h}{\partial x} \right)^2 \right) + \epsilon^2 (\tau_{zz} - \tau_{xx}) \frac{\partial h}{\partial x} = 0 \quad (2.13b)$$

and

$$\begin{aligned} -\epsilon p + \epsilon^2 \left[ \tau_{zz} + \epsilon^2 \tau_{xx} \left( \frac{\partial h}{\partial x} \right)^2 - \tau_{xz} \left( \frac{\partial h}{\partial x} \right) \right] \left[ 1 + \epsilon^2 \left( \frac{\partial h}{\partial x} \right)^2 \right]^{-1} \\ = \epsilon^3 \frac{1}{Ca} \frac{\partial^2 h}{\partial x^2} \left[ 1 + \epsilon^2 \left( \frac{\partial h}{\partial x} \right)^2 \right]^{-\frac{3}{2}}, \end{aligned} \quad (2.13c)$$

where  $Ca = \mu U / \gamma$  is the capillary number.

In nonlinear simulations, solving (2.11) at high  $De$  can lead to numerical instabilities. Methods to address such issues in viscoelastic flow have been reviewed by Alves *et al.* (2021). For instance, Sureshkumar & Beris (1995) introduced an artificial diffusive stress term to suppress instabilities, which necessitates specifying boundary conditions for the stress tensor. In our study, however, we do not perform nonlinear simulations and thus do not encounter numerical instabilities. Instead, we use linear stability analysis where, as we shall see in § 2.2, the stress tensor components can be directly determined in terms of velocity components or their spatial derivatives (see (2.19)).

## 2.2. Linear stability

Assuming stress-free side conditions at  $x = 0$  and  $x = 1$ , the governing equations (2.9)–(2.13) are perturbed around the base state, which is quiescent with respect to the moving frame of reference, using

$$\phi = \phi_0 + \phi_1 = \phi_0 + \sin kx e^{\sigma t} \sum_{n=-N}^{n=N} \hat{\phi}_n e^{(in\omega t)/2} \quad (2.14)$$

and

$$\psi = \psi_0 + \psi_1 = \psi_0 + \cos kx e^{\sigma t} \sum_{n=-N}^{n=N} \hat{\psi}_n e^{(in\omega t)/2}, \quad (2.15)$$

where  $\phi$  corresponds to the unknown dependent variables  $u$  and  $\tau_{xz}$  and  $\psi$  corresponds to  $w$ ,  $\tau_{xx}$ ,  $\tau_{zz}$ ,  $p$  and  $h$ . The subscript 1 denotes the infinitesimal disturbance with a wavenumber,  $k$ , and an inverse time constant,  $\sigma$ . The summation in (2.14) and (2.15) ensures compatibility with the parametric forcing term in (2.10b), with  $N$  denoting the number of oscillatory modes considered (Nayfeh 1981). The quiescent base state (denoted by subscript 0) is given by

$$u_0 = w_0 = 0, \quad \tau_{xx0} = \tau_{xz0} = \tau_{zz0} = 0, \quad -\frac{\partial p_0}{\partial z} = \mathcal{G} + \mathcal{A} \cos(\omega t) \text{ and } h_0 = 0. \quad (2.16)$$

Next, we substitute the forms given by (2.14), (2.15) and (2.16), into (2.9)–(2.13) and linearize these in terms of the amplitudes  $\hat{\phi}$  and  $\hat{\psi}$ . In the resulting equations, (2.17)–(2.23), which are written below, we have dropped for convenience the terminology related to the summation over the temporal modes, except for (2.23). Thus, we obtain

$$ku + \frac{\partial w}{\partial z} = 0, \quad (2.17)$$

$$\epsilon Re \left( \sigma + \frac{i\omega}{2} \right) u = \epsilon kp - \epsilon^2 k \tau_{xx} + \frac{\partial \tau_{xz}}{\partial z}, \quad (2.18a)$$

$$\epsilon^3 Re \left( \sigma + \frac{i\omega}{2} \right) w = -\epsilon \frac{\partial p}{\partial z} + \epsilon^2 k \tau_{xz} + \epsilon^2 \frac{\partial \tau_{zz}}{\partial z} \quad (2.18b)$$

and

$$\tau_{xx} + De \left( \sigma + \frac{i\omega}{2} \right) \tau_{xx} = 2ku, \quad \tau_{xz} + De \left( \sigma + \frac{i\omega}{2} \right) \tau_{xz} = \frac{\partial u}{\partial z} - \epsilon^2 kw \quad (2.19)$$

$$\text{and} \quad \tau_{zz} + De \left( \sigma + \frac{i\omega}{2} \right) \tau_{zz} = 2 \frac{\partial w}{\partial z}.$$

Equations (2.19) reflect the same constitutive relationship used by Müller & Zimmermann (1999), Kumar (1999) and Schön & Besthorn (2023). At the bottom wall,  $z = -1$ , we have

$$u = 0 \text{ and } w = 0 \quad (2.20)$$

and at the interface,  $z = 0$ , we have

$$\epsilon w = \epsilon \left( \sigma + \frac{i\omega}{2} \right) h, \quad (2.21)$$

$$\tau_{xz} = 0 \quad (2.22)$$

and

$$\sum_{n=-N}^{n=N} e^{(i\omega t)/2} \left\{ -\epsilon \hat{p}_n + \epsilon [\mathcal{G} + \mathcal{A} \cos(\omega t)] \hat{h}_n + \epsilon^2 \hat{\tau}_{zzn} + k^2 \epsilon^3 \frac{1}{Ca} \hat{h}_n \right\} = 0. \quad (2.23)$$

The above linearized equations are examined from two perspectives. In the first perspective,  $\mathcal{A}$  and  $\omega$  are set to zero and the set of the inverse time constants,  $\sigma$ , is then computed, observing that, in general,  $\sigma$  is complex. The real parts of  $\sigma$  are negative when the fluid is in a gravitationally stable configuration. The leading  $\sigma$  is the inverse time constant whose real part is the least negative among all complex  $\sigma$ . The imaginary part of the leading  $\sigma$  gives an estimate of the natural frequency of the system (Dinesh *et al.* 2023).



When a system is parametrically forced at its natural frequency, resonance-induced instability is known to occur (Kumar & Tuckerman 1994). Knowing how the real part of the leading  $\sigma$  behaves with  $De$  informs us on how the threshold of the instability behaves. The more negative the leading  $\sigma$ , the higher the threshold of the resonance-induced instability. To obtain analytical expressions on the behaviour of  $\sigma$  with  $De$  we appeal to a reduced-order model (the derivation of which is given in Appendix A).

In the second perspective, the dimensionless forcing amplitude,  $\mathcal{A}$ , is calculated by setting  $\sigma$  to zero and expressing the dependent variables in terms of the interface deflection,  $h$  (Kumar & Tuckerman 1994). This results in an eigenvalue problem arising from (2.23) and takes the form

$$\mathbf{C}\mathbf{x} = \mathcal{A}\mathbf{D}\mathbf{x}, \quad (2.24)$$

with eigenvalues,  $\mathcal{A}$ , and eigenvectors  $\mathbf{x} = \{\hat{h}_N, \hat{h}_{N-1} \dots \hat{h}_{-N}\}$ . The detailed forms of the matrices,  $\mathbf{C}$  and  $\mathbf{D}$ , are provided in Appendix B. It should be noted that the eigenvalues will appear in pairs as  $\pm\mathcal{A}$  on account of the periodic forcing term given in (2.2). We therefore take  $\mathcal{A}$  to be positive without any loss of generality. The solutions to the eigenvalue problem (2.24) are numerically obtained using the Eigenvalue routine in Mathematica<sup>®</sup>. The neutral stability curves,  $\mathcal{A}$  versus  $k$ , thus obtained are used to examine the effect of viscoelasticity on the resonant or Faraday instability. These calculations are done by relaxing the assumption of small  $\epsilon$ , thereby allowing consideration of arbitrary wavenumbers,  $k$ . This is done by using a common length scale,  $d^*$ , which amounts to scaling the horizontal direction with  $d^*$  and setting  $\epsilon = 1$  in the scaled forms given in (2.8).

The threshold amplitude, numerically obtained using (2.24), can also be obtained accurately for low wavenumbers by appealing to a reduced-order model (assuming  $\epsilon \ll 1$ ) derived in Appendix A. The advantage of this model is that it provides explicit relations for  $\sigma$  and  $\mathcal{A}$  as functions of the wavenumber,  $k$ , without having to determine the eigenfunctions. We now briefly discuss the main results arising from such a model.

### 2.3. A brief discussion on the reduced-order model

The reduced model is obtained upon dropping terms of  $O(\epsilon^2)$  in (2.17) to (2.23) and integrating (2.17) to (2.19) along the  $z$ -direction using (2.20) to (2.23) (Kalliadasis *et al.* 2011). The model yields the following dispersion relation (cf. (A20))

$$\sum_{n=-N}^{n=N} e^{(in\omega)/2} \left\{ \left[ 1 + \left( \sigma + \frac{in\omega}{2} \right) De \right] \left[ \frac{2}{5} \left( \sigma + \frac{in\omega}{2} \right)^2 Re \hat{h}_n \right. \right. \\ \left. \left. + \frac{1}{3} \left( \mathcal{G}k^2 + \frac{1}{Ca} k^4 \right) \hat{h}_n + \frac{1}{3} \mathcal{A} \cos(\omega t) k^2 \hat{h}_n \right] + \left( \sigma + \frac{in\omega}{2} \right) \hat{h}_n \right\} = 0. \quad (2.25)$$

To get an algebraic expression that yields the inverse time constants,  $\sigma$ , for a system subject to momentary disturbance, we set  $\mathcal{A} = 0$  and  $\omega = 0$  in (2.25), divide by  $a$  and obtain

$$(aDe) \left( \frac{\sigma}{a} \right)^3 + \left( \frac{\sigma}{a} \right)^2 + \left( 1 + \left[ \frac{b}{a} \right] (aDe) \right) \left( \frac{\sigma}{a} \right) + \left[ \frac{b}{a} \right] = 0, \quad (2.26)$$

where the parameters  $a$  and  $b$  are given by

$$a = \frac{5}{2} \frac{1}{Re} \text{ and } b = \frac{1}{3} \left( \frac{k^4}{Ca} + k^2 \mathcal{G} \right). \quad (2.27)$$



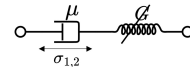
Solutions to the characteristic equation for inverse time constant,  $\sigma$  (cf. [Appendix A](#)),

$$(aDe) \left( \frac{\sigma}{a} \right)^3 + \left( \frac{\sigma}{a} \right)^2 + \left( 1 + \left[ \frac{b}{a} \right] (aDe) \right) \left( \frac{\sigma}{a} \right) + \left[ \frac{b}{a} \right] = 0. \quad (3.1)$$

In the limit  $k \rightarrow 0$ , (3.1) becomes

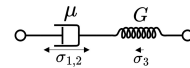
$$(aDe) \left( \frac{\sigma}{a} \right)^3 + \left( \frac{\sigma}{a} \right)^2 + \left( \frac{\sigma}{a} \right) = 0. \quad (3.2)$$

(a)  $De = 0$ :  $\sigma_1/a = 0$ ,  $\sigma_2/a = -1$



(b) Small  $De$ :

$\sigma_1/a = 0$ ,  $\sigma_2/a = -1 - aDe + O(aDe)^2$ , and  $\sigma_3/a = -1/(aDe) + 1 + aDe + O(aDe)^2$



(c) Large  $De$ :  $\sigma_1/a = 0$ , and  $\sigma_{2,3}/a = -1/(2aDe) \pm i\sqrt{1/(aDe) - 1/(2aDe)^2}$

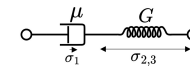


Table 1. Inverse-time constants at  $\mathcal{A} = 0$  and  $k = 0$  for different  $De$  limits. Parameters  $a$  and  $b$  are given by (2.27).

Observe that the terms  $(aDe)$ , i.e.  $(5/2)(De/Re)$ ,  $(\sigma/a)$  and  $(b/a)$  are independent of the characteristic time. The solutions to (2.26) for the inverse time constants are presented in [table 1](#).

To get an algebraic expression determining the critical amplitude,  $\mathcal{A}$ , for the dominant harmonic response, we set  $\sigma = 0$  in (2.25) and then employ a truncated Floquet expansion up to three terms for  $n = 2, 0$  and  $-2$ , yielding (cf. (A26))

$$\mathcal{A} = \sqrt{6 \left( \frac{1}{Ca} + \frac{G}{k^2} \right) \frac{[(\omega + De\omega c)^2 + c^2]}{(1 + De^2\omega^2)c + De\omega^2}}, \quad (2.28)$$

where  $c = b - \omega^2/a$ . In addition, this expression is used to provide useful insight into the interface's temporal response as well as the stability characteristics of gravitationally unstable systems undergoing parametric forcing.

### 3. Effect of elasticity on the fluid's damping

The role of elasticity on the fluid's damping can be understood by visualizing its behaviour as a simple spring–dashpot system (illustrated in [table 1](#)), with the stress–strain relationship given by (2.19). The viscoelastic fluid consists of a viscous component with viscosity,  $\mu$ , represented by the dashpot, while the elastic component of shear modulus,  $G$ , is represented by the spring. When the fluid system is subjected to a disturbance, the strain is distributed between the viscous and elastic components. If the value of  $G$  is large, i.e. at small values of Deborah numbers, the elastic component stores substantial normal and shear stresses while undergoing minimal deformation. Consequently, the main part of the deformation is undergone by the dashpot, leading to enhanced damping, dissipating the

stresses acting on the system and thus stabilizing it. Conversely, at small values of  $G$  or large Deborah numbers, the elastic component deforms more readily and the deformations undergone by the viscous component are reduced, thereby decreasing overall damping within the system. In the following section, we substantiate these statements by examining the values of the leading  $\sigma$  for  $\mathcal{A} = 0$  for different values of  $G$  by considering three cases:  $De = 0$  (a Newtonian fluid); small Deborah numbers (i.e. a weakly elastic fluid); large Deborah numbers (i.e. a dominantly elastic fluid).

### 3.1. Newtonian fluids: $De=0$

Analytical solutions for  $\sigma$  in the case of a Newtonian liquid can be obtained by setting  $De = 0$  in the characteristic equation (3.1) given in table 1 and solving for the resulting quadratic roots. This yields

$$\frac{\sigma_{1,2}}{a} = -\frac{1}{2} \pm i\sqrt{\frac{b}{a} - \frac{1}{4}}, \quad (3.3)$$

where the real part of  $\sigma/a$ , which is independent of the characteristic time, gives the decay rate of the disturbances and the imaginary part, its natural frequency.

Observe that for gravitationally stable configurations, i.e. when  $b/a > 0$ , both roots have a negative real part. Such a system is stable due to the viscous dissipative effects that dampen all disturbances. However, for gravitationally unstable configurations, i.e. when  $b/a < 0$ , we obtain two real roots, one root being positive, other being negative. The interface of such a system grows with time.

### 3.2. Viscoelastic fluids: $De \neq 0$

If  $De \neq 0$ , the characteristic cubic equation (3.1) exhibits three solutions, where the additional  $\sigma$  arises from the time derivative in the stress-strain constitutive equation (2.19). While solutions to these cubic equations may be rigorously obtained, we can easily derive expressions for the real parts of  $\sigma$  in the limit  $k \rightarrow 0$ . These expressions, also given in table 1, will be employed to elucidate the impact of elasticity on the fluid's damping in the next two subsections.

#### 3.2.1. Low Deborah numbers or weakly elastic fluids

Consider the effect of elasticity for small Deborah numbers. Recall, from the example of a spring–dashpot system that, at small  $De$ , damping is enhanced. This is evident by the trends shown by  $\sigma_1$  and  $\sigma_2$  in the limit  $k \rightarrow 0$  (cf. table 1(b)) and depicted in figure 2(a) where we plot the real part of  $\sigma/a$ , denoted  $Re(\sigma/a)$ , versus  $(aDe)$ , two quantities that are independent of the characteristic time. The root,  $\sigma_3$ , is real and negative, the implication being it cannot influence an oscillatory Faraday instability threshold when the system is subjected to parametric forcing. However, we can see by computations that  $\sigma_1$  and  $\sigma_2$ , although real as  $k \rightarrow 0$ , become complex conjugates beyond a threshold wavenumber,  $k$ , that depends on the value of  $(aDe)$ ,  $(\mathcal{G}/a)$  and  $aCa$ , quantities that are also independent of the characteristic time. This result is depicted in figure 2(b). Observe that as  $k$  approaches zero,  $\sigma_1$  approaches zero and  $\sigma_2$  becomes more negative as  $De$  increases, implying that overall damping within the system increases with an increase in elasticity. This behaviour continues even when  $k$  is increased and  $\sigma_{1,2}$  become complex, thereby showing an increase in the Faraday instability threshold for an increase in  $De$  in the low Deborah number regime.

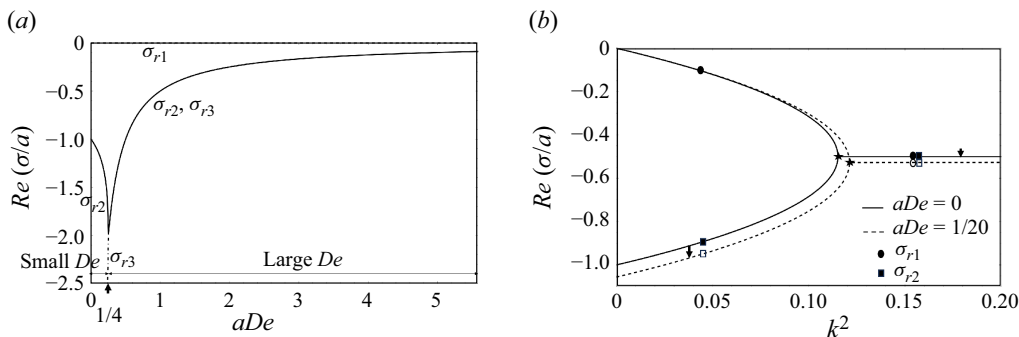


Figure 2. (a) The real part of  $\sigma/a$ , denoted  $Re(\sigma/a)$ , versus  $aDe$  from (3.2). The arrow denotes the location beyond which  $\sigma_2$  and  $\sigma_3$  become complex conjugates. (b) Here  $Re(\sigma/a)$  versus  $k^2$  for two different values of  $(aDe)$  in low Deborah number regime for parameters  $aCa = 5.3$  and  $\mathcal{G}/a = 0.63$ , corresponding to the properties of a fluid given in table 2. The inverse time constant,  $\sigma_3$ , which has very large negative values at low  $De$  is not shown here. The symbol  $\star$  denotes the location beyond which  $\sigma_1$  and  $\sigma_2$  become complex conjugates.

Physical property	Symbol	Value
Viscosity	$\mu$	0.28 Pa s
Shear modulus	$G$	1.55 Pa
Density	$\rho$	1000 kg m <sup>-3</sup>
Surface tension	$\gamma$	0.074 N m <sup>-1</sup>
Film thickness	$d^*$	$5 \times 10^{-3}$ m

Table 2. Physical parameters used in the calculations. Fluid properties correspond to 0.5 % wt./vol. aqueous polyacrylamide solution (Sobti *et al.* 2018) making  $De/Re = 2$ , which is independent of any time scale.

### 3.2.2. Large Deborah numbers or strongly elastic fluids

Contrasting the case of a low Deborah number with that of large  $De$ , we observe that now the decay rates decrease with an increase in  $De$ . This is depicted in figure 2(a) and supported by the equations given in case (c) of table 1, from which we also see that when  $(aDe) > 1/4$ , i.e.  $De/Re > 1/10$ ,  $\sigma_2$  and  $\sigma_3$  are complex conjugates, their real parts being inversely proportional to  $De$ . Therefore, for large  $De$ , the elasticity-induced inertia reduces the stability of the system, i.e. making it more susceptible to Faraday instability.

The behaviour of  $\sigma$  values with  $De$  as discussed above and its implication in Faraday instability is delineated in two cases. These are parametric forcing on a gravitationally stable system and forcing on a gravitationally unstable system. We turn to these two cases in the following sections.

## 4. Parametric forcing of a viscoelastic fluid in a gravitationally stable orientation

### 4.1. Relating the behaviour of the Faraday instability to the inverse time constants

In the last section, it was hypothesized that damping rates ought to be connected to the stability threshold of resonant instability. To verify this, we examine the stability characteristics by considering a viscoelastic fluid whose properties are given in table 2, focusing on the case of a gravitationally stable system where  $g = 9.8 \text{ m s}^{-2}$ , i.e. Earth's

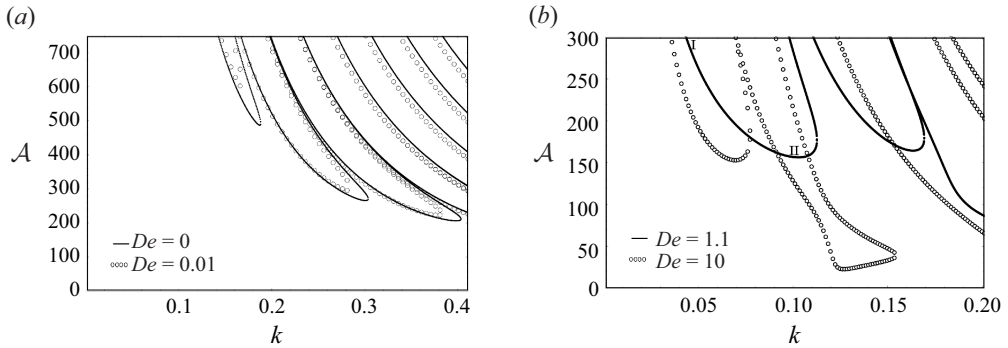


Figure 3. Critical  $\mathcal{A}$  versus  $k$  curves, shows the effect of elasticity on the Faraday instability threshold at  $g = 9.8 \text{ m s}^{-2}$ . (a) The solid curve represents  $De = 0$  and the open circle markers represent  $De = 0.01$  (b) The solid curve  $De = 1.1$  and the open circle markers represent  $De = 10$ . The dimensional frequency,  $\omega^* = 2\pi \text{ rad s}^{-1}$  and  $f^* = 1 \text{ Hz}$ .

gravity level. Linear stability calculations are performed using the complete set of equations (2.17) to (2.23) for arbitrary wavenumbers,  $k$ .

In a weakly viscoelastic fluid, we noted in § 3 that there is increased damping due to elasticity. This, in turn leads to increased threshold amplitudes for the onset of Faraday instability as illustrated in the  $\mathcal{A}$  versus  $k$  graphs of figure 3(a). These graphs are plotted for two different values of Deborah number in the low Deborah number region, *viz.*,  $De = 0$  and  $De = 0.01$ , reflecting a change only in the shear modulus in table 2. Henceforth we take the characteristic velocity to be

$$U \equiv d^* \omega^*, \quad (4.1)$$

thus requiring the scaled frequency to be  $\omega = 1$ , from (2.8).

By contrast with a low  $De$  region, we observed in § 3 that at large  $De$  there is a decrease in the damping rate with an increase in  $De$  (cf. figure 2a). This implies that the threshold amplitude for the Faraday instability ought to decrease with an increase in  $De$  due to the inertia-like action provided by elasticity. This is illustrated by the results in figure 3(b). A significant reduction in critical amplitude is shown for this case in the figure where  $\mathcal{A}$  versus  $k$  is plotted for two different values of Deborah numbers, *viz.*,  $De = 1.1$  and  $De = 10$ . The value  $G = 1.55 \text{ Pa}$  given in table 2 for a realistic fluid corresponds to  $De = 1.1$ , placing it within the large Deborah number category. Observe in figure 3(b) that there is a noticeable difference in the shape of the second tongue and subsequent tongues (not shown), as we transit from  $De = 1.1$  to  $De = 10$ , where the elasticity of the fluid becomes dominant. This difference is attributed to the memory effect imparted by the fluid's elasticity as characterized by the change in the relaxation time of the fluid. The core characteristics of the stability curves, however, remain unchanged, such as the alternating subharmonic and harmonic responses.

#### 4.2. The temporal response of the interface due to Faraday instability

Just as the real part of  $\sigma$  informs us about the behaviour of the Faraday threshold, the imaginary part of  $\sigma$  provides information about the interface's temporal response. Recall, from the earlier section that we obtain three roots to  $\sigma$  when (3.1) is solved, yielding two complex conjugate roots and one purely negative root, for a wavenumber,  $k$ , above a minimum value as depicted in figure 2(b). The very existence of complex  $\sigma$  suggests the possibility of an oscillatory response upon resonant instability, as observed in the case

of Newtonian fluids (Kumar & Tuckerman 1994). On the other hand, the presence of a purely negative  $\sigma$ , indicates the possibility of a monotonic response. We shall show that such a response is indeed possible and becomes dominant compared with an oscillatory instability for large  $De$  as gravity approaches zero.

To determine the temporal response of the instability we revisit the  $\mathcal{A}$  versus  $k$  graph represented by the solid curve in figure 3(b), i.e. for  $De = 1.1$  and  $g = 9.8 \text{ m s}^{-2}$ . The graph depicts a critical curve consisting of multiple ‘tongues’, each associated with distinctive temporal modes. Typically, the interface response at the onset of instability corresponds to the temporal mode with the lowest of all the critical amplitudes. The nature of the temporal response of the interface at a given critical amplitude,  $\mathcal{A}$ , is determined by examining the coefficients,  $\hat{h}_n$ , in the Floquet summation (2.24). If the dominant coefficient corresponds to  $n = 0$ , the response is said to be monotonic. Otherwise, it is an oscillatory response. Among the oscillatory modes, depending on whether the dominant coefficient is odd or even, the interface response is either subharmonic or harmonic. We note that higher-order subharmonics may occur when the dominant coefficient corresponds to  $n = 3, 5, 7$ , etc. And higher-order harmonics may occur when  $n = 4, 6, 8$ , etc. As an example, the response of the interface deformation is subharmonic at the minimum of the second tongue (cf. solid curves in figure 3b) as all the even coefficients are zero and the indices of the dominant coefficients are odd. On the other hand, the response of the interface deformation at the minimum of the first tongue is harmonic as all the odd coefficients are zero and the indices in the dominant coefficients are even. Although not displayed in figure 3(b), our calculations show that for  $De \sim 1$ , we observe a transition between subharmonic and harmonic responses, in agreement with earlier works (Kumar 1999; Müller & Zimmermann 1999). It is noteworthy that earlier workers have also observed a harmonic response in parametric forcing in the case of soft solids (Bevilacqua *et al.* 2020).

The relative importance of a monotonic response with respect to a first harmonic response in the first tongue may be estimated from the ratio obtained using a three-term Floquet summation of the reduced-order model, i.e. when  $\epsilon \ll 1$ . The details of such a model are given in Appendix A, where, from (A27) we obtain

$$\frac{\hat{h}_0}{\hat{h}_2 + \hat{h}_{-2}} = \frac{\mathcal{A}}{2 \left( \frac{k^2}{Ca} + \mathcal{G} \right)}. \quad (4.2)$$

The corresponding critical amplitude,  $\mathcal{A}$ , obtained from (2.28), is given by

$$\mathcal{A} = \sqrt{6 \left( \frac{1}{Ca} + \frac{\mathcal{G}}{k^2} \right) \frac{[(1 + cDe)^2 + c^2]}{(1 + De^2)c + De}}, \quad (4.3)$$

where  $c(k) = b(k) - \frac{1}{a}$ , and where  $a$  and  $b$  are given by (2.27). Recall that the dimensionless frequency,  $\omega$ , is equal to one. Observe that as  $k$  goes to zero, the ratio  $\hat{h}_0/(\hat{h}_2 + \hat{h}_{-2})$  and the critical amplitude,  $\mathcal{A}$ , approach infinity provided  $\mathcal{G} > 0$ . In figure 3(b), this region, where the monotonic mode is dominant corresponds to the descending region in the first critical curve, denoted I. However, as  $k$  increases, i.e. as we approach the minima of the first critical curve, denoted II, the harmonic modes become important. It should be noted that the monotonic behaviour for curves characterized by  $De = 1.1$  will also occur for curves with different shear moduli,  $G$ , but at a different parametric frequency.

Now, as  $\mathcal{G}$  is reduced, the region I of the curve shifts downward faster than the region II and all other regions, subsequently becoming the most unstable mode with the lowest

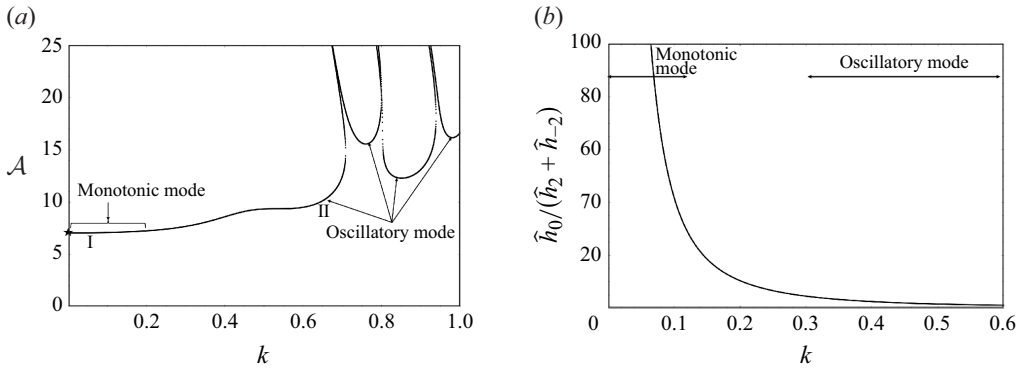


Figure 4. The existence of a monotonic Faraday instability mode, depicted by graphs using the properties of the fluid given in table 2 with  $\mathcal{G} = 0$  (a) Critical  $\mathcal{A}$  versus  $k$ . (b) The ratio  $\hat{h}_0/(\hat{h}_2 + \hat{h}_{-2})$  versus  $k$  obtained using (4.2). The dimensional frequency,  $\omega^* = 2\pi \text{ rad s}^{-1}$  and  $f^* = 1 \text{ Hz}$ .

critical amplitude at  $\mathcal{G} = 0$ . This is illustrated in figure 4(a) where the lowest amplitude corresponds to the point where the curve touches the ordinate (marked by a star), i.e.  $k = 0$ . Indeed, the ratio  $\hat{h}_0/(\hat{h}_2 + \hat{h}_{-2})$  versus  $k$  graph plotted in figure 4(b) shows that the monotonic behaviour of the system increases with a decrease in wavenumber and eventually becomes purely monotonic at  $k = 0$ . The critical amplitude as  $k$  approaches zero can be accurately determined using the expression for  $\mathcal{A}$  from (4.3). This expression is in good agreement with figure 4(a) in the limit of small wavenumbers (see the figure in Appendix A).

#### 4.3. Criteria for the existence of a purely monotonic faraday instability at $\mathcal{G} = 0$

The criteria for the existence of purely monotonic instability can be derived by requiring that  $De$  and  $Re$  be such that (4.3) yields a real value of  $\mathcal{A}$  as  $k \rightarrow 0$ . Doing this results in the criteria taking the form

$$\frac{De}{1 + De^2} > \frac{2}{5} Re, \quad (4.4)$$

an inequality that is derived in Appendix A (cf. (A29)). It can be observed from (4.4) that the left-hand side reaches a maximum at  $De = 1$ , i.e. when the forcing frequency is the inverse of the relaxation time. At this value of  $De$ , the left-hand side of (4.4) is  $1/2$  and  $Re < 5/4$ . Thus, to get a monotonic mode,  $Re$  must depend on this condition but must not exceed  $5/4$ , i.e. the inertia due to momentum must be weak.

At high  $Re$ , such that (4.4) is not satisfied, the fluid interface exhibits oscillatory behaviour because the viscous damping within the system is reduced. However, even at low  $Re$ , i.e. if  $Re < 5/4$ , but high  $De$  i.e. if  $De > 1$ , (4.4) will also not be satisfied and the response of the interface will be oscillatory because of the elasticity-induced inertia.

We can use the criteria given in the relationship given by (4.4), to determine bounds on  $G$ ,  $\mu$  and  $\omega^*$ . As an example, for assigned values of  $\mu$ ,  $\omega^*$ , etc., we can obtain  $G$  from  $De$  by a rearrangement of relationship (4.4), viz.

$$\frac{5}{4Re} - \sqrt{\frac{25}{16Re^2} - 1} < De < \frac{5}{4Re} + \sqrt{\frac{25}{16Re^2} - 1}. \quad (4.5)$$

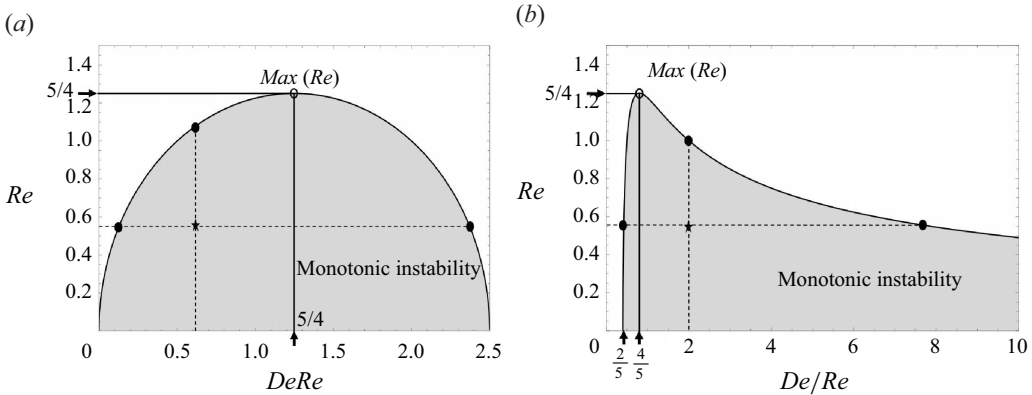


Figure 5. Phase diagrams illustrating the parameter ranges within which a purely monotonic mode exists at  $G = 0$ . (a) Here  $Re$  versus  $DeRe$ , determining the bounds of  $\mu$  for fixed  $G$  and  $\omega^*$  from (4.6). (b) Here  $Re$  versus  $De/Re$ , determining the bounds of  $\omega^*$  for a fixed  $G$  and  $\mu$  from (4.7).

Likewise, we can obtain  $\mu$  from  $Re$  with another rearrangement of (4.4), i.e.

$$\sqrt{\frac{5}{2}(ReDe) - (ReDe)^2} > Re \quad (4.6)$$

for assigned values of  $G$ ,  $\omega^*$ , etc. Finally, for assigned values of  $\mu$ ,  $G$ , etc., we may estimate the values of the dimensional frequency,  $\omega^*$ , from  $Re$  with one more rearrangement of (4.4) as

$$\frac{\sqrt{\frac{5}{2}\frac{De}{Re} - 1}}{\frac{De}{Re}} > Re \quad (4.7)$$

observing that  $De/Re$  is independent of  $\omega^*$ . These bounds on  $G$ ,  $\mu$  and  $\omega^*$  are also illustrated using the phase diagrams shown in figures 5(a) and 5(b). In both graphs, the intersection of the horizontal and vertical dashed lines marked by '★' indicates the parameter values used to generate figure 4(a), depicting the presence of a purely monotonic mode. Observe that the maximum value of  $Re$ ,  $Re = 5/4$ , above which monotonic instability cannot occur, a result that we derived earlier from (4.4), is also denoted on figures 5(a) and 5(b).

Using the properties of a viscoelastic fluid given in table 2 in the relationship (4.7), we can see that the pure monotonic mode occurs for frequencies of forcing, less than 1.8 Hz. This cutoff frequency can also be obtained from the graph in figure 5(b) by calculating  $\omega^*$  from  $Re$  at  $De/Re = 2$  (marked by ●). Beyond this frequency, pure monotonic instability does not exist, though a predominantly monotonic response is still observed near this critical frequency. As the forcing frequency is increased further, the instability response changes to a dominantly oscillatory behaviour.

To ensure that disturbances are in the low wavenumber limit, the finiteness of the container must be taken into account. For example, in containers of finite width,  $W$ , and with stress-free sidewalls, we have a set of allowable wavenumbers,  $k$ , where  $k = m\pi/W$ , with  $m \in \mathbb{N}$ . Consequently, in a narrow container, only shorter waveforms leading to oscillatory instability will occur as the permissible wavenumber belongs to the large wavenumber region (cf. figure 4a). However, in wide containers long wavelength waveforms will develop, leading to a dominantly monotonic instability.



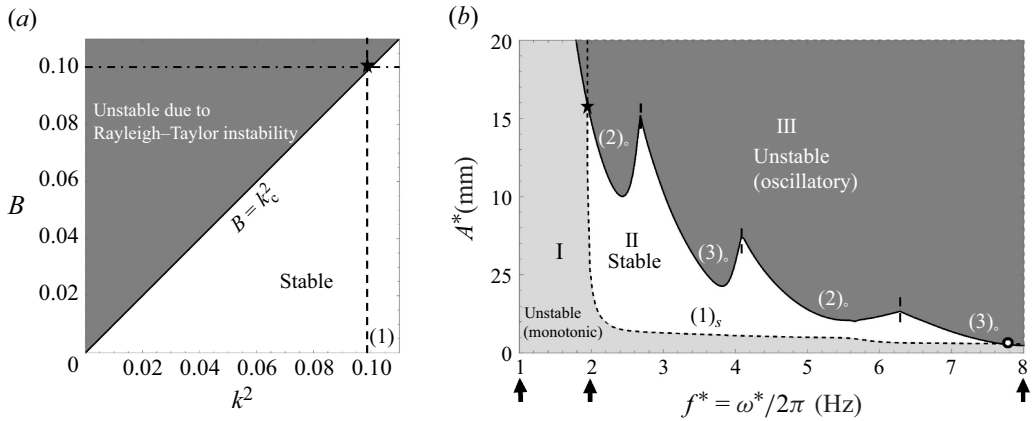


Figure 6. Viscoelastic fluid layer in an RT arrangement (a) without forcing – neutral stability curve. The point  $\star$  is the intersection between  $B = 0.1$  and  $k = \pi/W$  (the first allowable wavenumber) and lies slightly above the neutral line (b) with forcing – stability bounds for the monotonic (s) and oscillatory (o) modes for  $B = 0.1$ , width  $W = 10$ ,  $De/Re = 2$ . Integers between parentheses, ( $m$ ), identify the most unstable wavenumber  $k = m\pi/W$ . The two critical frequencies,  $f_{c1}^*$  and  $f_{c2}^*$ , are marked  $\star$  and  $\circ$ , occurring where dashed and solid curves intersect.

The occurrence of a monotonic response, a new observation in parametric forcing of viscoelastic fluids is thus attributed to the inverse time constant,  $\sigma$ , which is purely real. It might be of related interest to note that other monotonic long-wave instabilities, such as the Rayleigh–Taylor (RT) instability of Newtonian fluids, are also characterized by purely real  $\sigma$ . Further, such an instability may be stabilized by parametric forcing (Sterman-Cohen *et al.* 2017). This therefore encourages the question: Can the RT instability of a viscoelastic fluid be staved off upon parametric forcing? To answer this question we set  $\mathcal{G}$  to be negative, i.e. with gravity now pointing upwards in figure 1, fix the container width, and then analyse the regions of stability/instability when parametric forcing is employed.

## 5. Parametric forcing of a viscoelastic fluid in a gravitationally unstable orientation

A fluid that is in a gravitationally unstable configuration may be stabilized by restricting the disturbances to short enough wavelengths such that the surface tension force exceeds the gravitational force. This is the familiar RT problem (Chandrasekhar 1961). The neutral stability threshold is given by  $B = k_c^2$  and depicted in figure 6(a), where  $k_c$  is the cutoff wavenumber. Here,  $B$  is the Bond number, given by  $B = -\mathcal{G}Ca$ , where  $B > 0$  and  $\mathcal{G} < 0$ , due to the reversal in direction of the gravity vector from that shown in figure 1. The relationship between  $B$  and  $k_c^2$  depicted in figure 6(a) is unaffected by the fluid's elasticity as observed from (2.17)–(2.23), when  $\sigma$ ,  $\mathcal{A}$  and  $\omega$  are set to zero. Above the critical line in figure 6(a), the fluid system is unstable. Therefore, in an unbounded container, the most unstable wavenumber is  $k = 0$  and we always have instability. However, in finite-width containers, as noted earlier, the lowest allowable wavenumber is  $k = \pi/W$ , marked by a vertical dashed line in figure 6(a). For Bond numbers less than  $k^2|_{m=1}$ , we have stability.

It is known from earlier work that a Newtonian fluid in a RT unstable configuration can be stabilized by parametric forcing (Sterman-Cohen *et al.* 2017). Because the Faraday instability is inertia-driven, the transient nature of the stress–strain constitutive relationship in a viscoelastic fluid must necessarily affect the manner in which parametric forcing can stabilize an otherwise RT unstable configuration. In this section, we therefore discuss the effect of such forcing on a viscoelastic fluid layer whose properties are given in table 2.

To understand the salient features of parametric stabilization of our gravitationally unstable system we turn to [figure 6\(b\)](#), which depicts forcing amplitude versus frequency for an example case where  $W = 10$  and  $B = 0.1$ . The critical curves in [figure 6\(b\)](#) are displayed in dimensional form in order to show that the results are in a practically achievable range. The curves in the figure are obtained by computing the two lowest critical amplitudes amongst all allowable wavenumbers for each input parametric frequency. The critical values are then sorted based on their temporal response, the dashed curve indicating the monotonic mode denoted,  $\mathcal{A}_s$ , where  $s$  represents a steady or monotonic mode. The solid curves represent oscillatory modes with critical amplitudes denoted,  $\mathcal{A}_o$ . These curves divide the  $A^*$  versus  $f^*$  graph into three regions of stability/instability, where  $f^* = \omega^*/2\pi$ . Below the dashed curve, the viscoelastic fluid system is monotonically unstable, and above the solid curve, it will exhibit an oscillatory response. Outside of these regions, there exists a stable region (white region), with a finite range in amplitude, lying between two critical frequencies (marked by  $\star$  and  $\circ$ ), where the dashed and solid curves intersect. Below the first critical frequency, denoted  $f_{c1}^*$ , the system is always unstable. Observe that  $f_{c1}^* = 1.9$  Hz is very close to the frequency  $f^* = 1.8$  Hz, below which a monotonic Faraday instability in the absence of gravity was predicted in § 4.3.

To understand the origin of  $f_{c1}^*$  (marked by  $\star$  in [figure 6b](#)), we turn to [figures 7\(a\)](#) and [7\(b\)](#) where we graph the  $\mathcal{A}$  versus  $k$  critical curves plotted for two frequencies on either side of  $f_{c1}^*$ , say  $f^* = 1$  Hz and  $f^* = 2$  Hz, marked by vertical arrows in [figure 6\(b\)](#). Let us focus on the low wavenumber regime near  $k = k_c$  (marked by upward arrows in [figures 7a](#) and [7b](#)), where we have a predominantly monotonic mode. The allowable wavenumbers are represented using vertical dotted lines in both figures. At  $\mathcal{A} = 0$ , the system is unstable to all wavenumbers to the left of  $k_c$  (marked by an upward arrow in [figure 7a](#)), implying that the waveform  $k|_{m=1}$ , i.e. a half-wave is unstable. At a frequency of  $f^* = 1$  Hz, this waveform remains unstable as we increase the forcing amplitude. Beyond a threshold amplitude, two half-waves become unstable but with an oscillatory response. On the other hand, at a frequency of  $f^* = 2$  Hz, the system transitions to a stable quiescent state at a critical amplitude of forcing,  $\mathcal{A}_s$ , before it advances to the onset of oscillatory instability at a critical amplitude  $\mathcal{A}_o$  (greater than  $\mathcal{A}_s$ ), upon further increase in amplitude.

A prediction of  $f_{c1}^*$  can be estimated by considering the relationship between  $\mathcal{A}^2$  and  $k^2$  at  $k = k_c$ , where  $\mathcal{A} = 0$ . This is done by appealing to the expression from the long-wave analysis given in (4.3). Prior to doing so, we first observe that if the curvature of the graph at  $k = k_c$  is negative and its slope is infinite, as depicted in [figure 7\(a\)](#), then the parametric forcing is of a destabilizing character. However, if the curvature is positive with an infinite slope, now depicted in [figure 7\(b\)](#), the parametric forcing has a stabilizing effect.

Therefore,  $f_{c1}^*$  signals the transition of the parametric forcing from a destabilizing to a stabilizing regime. Its value can be determined from (4.3) by evaluating

$$\left. \frac{d\mathcal{A}^2}{dk^2} \right|_{k=k_c} = \left. \frac{\mathcal{A}}{k} \frac{d\mathcal{A}}{dk} \right|_{k=k_c} = \left( -\frac{\mathcal{G}}{k_c^4} \right) \frac{[(1 + De)c]^2 + c^2}{(1 + De^2)c + De}, \quad (5.1)$$

and setting its reciprocal to zero, upon noting that  $b = 0$  and  $c = -(2/5)Re$  for  $k = k_c$ . Observe that (5.1) is positive when the denominator is positive. This criterion is exactly satisfied when (4.4) is satisfied, for which monotonic Faraday instability occurs in the case of zero gravity.

Let us now consider how  $f_{c1}^*$  changes with elasticity. To do this, we employ (4.7) and draw [figure 8](#), which implicitly depicts the dependence of  $f_{c1}^* = \omega_{c1}^*/2\pi$  on elasticity,

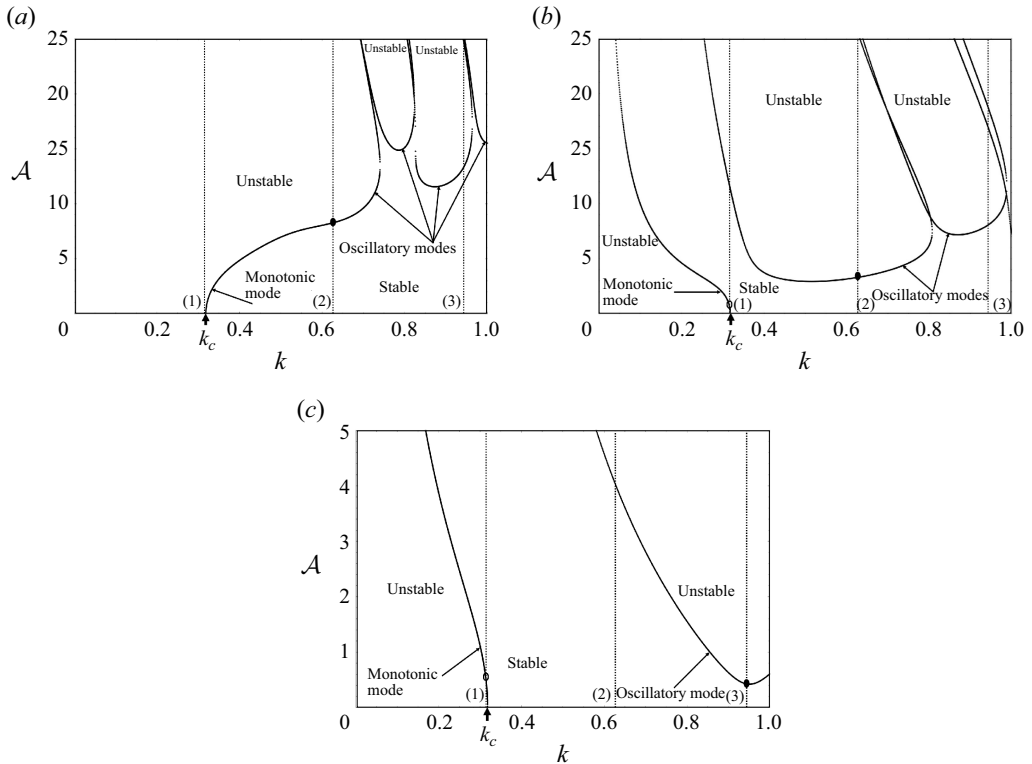


Figure 7. Here  $\mathcal{A}$  versus  $k$  curves obtained at frequencies (a)  $f^* = 1$  Hz, (b)  $f^* = 2$  Hz and (c)  $f^* = 8$  Hz illustrating the existence of two critical frequencies. Panels (a) and (b) illustrate the presence of the first critical frequency,  $f_{c1}^*$ . Panels (b) and (c) demonstrate the presence of the second critical frequency,  $f_{c2}^*$ . The symbol  $\circ$  represents  $\mathcal{A}_s$  and the symbol  $\bullet$  represents  $\mathcal{A}_o$ . The vertical dotted lines represent the permissible wavenumbers.

i.e.  $1/G$ . The scaled frequency is expressed here as  $Re_{c1} = \omega_{c1}^* \times (d^{*2}\rho/\mu)$  and the scaled elasticity is expressed as  $De/Re = (1/G) \times (\mu^2/d^{*2}\rho)$ , assuming  $\rho$ ,  $\mu$  and  $d^*$  are held fixed. Equation (4.7) reveals that the lowest permissible value of  $De/Re$  is  $2/5$ . We also see from (4.7) that  $Re_{c1}$  increases to a maximum value of  $5/4$  when  $De/Re$  is  $4/5$ . This implies that at the maximum,  $Re_{c1} \times (De/Re) = \omega_{c1}^* \times (\mu/G) = 1$ . That is, at the maximum, the critical frequency is equal to the inverse of the relaxation time. The decrease in  $Re_{c1}$  after the maximum is due to the inertial effects provided by elasticity. Further increase in  $De/Re$  cause  $Re_{c1}$  to approach zero as  $De/Re \rightarrow \infty$ .

In summary, the first critical frequency approaches zero at the low end of  $De/Re$  due to inertial action by momentum and at the high end of  $De/Re$  due to elastic effects. As illustrated by the phase diagram, figure 8, parametric forcing cannot stabilize a gravitationally unstable system below the curve, whereas above the curve, parametric forcing can stabilize an otherwise gravitationally unstable system. This sets apart the behaviour of the viscoelastic case from the Newtonian case, for which the first critical frequency is completely absent. We now turn to the second critical frequency.

The second critical frequency, denoted  $f_{c2}^*$  and marked by  $\circ$  in figure 6(b) is defined as the frequency beyond which stabilization cannot be achieved. This frequency is greatly influenced not only by  $De/Re$  but also by the Bond number,  $B$ . Its origin can be determined by comparing the  $\mathcal{A}$  versus  $k$  critical curves plotted for two frequencies

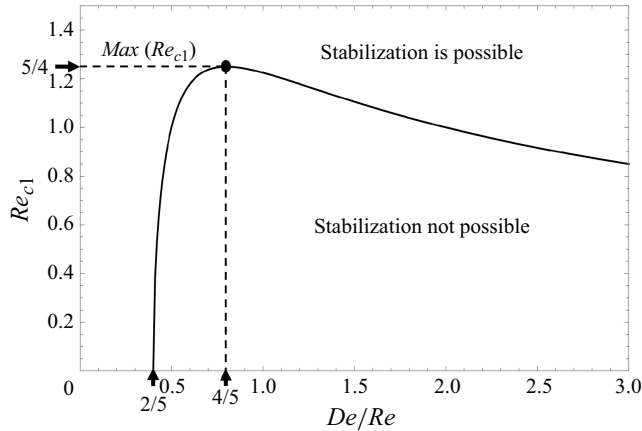


Figure 8. Phase diagram depicting the first critical frequency,  $f_{c1}^* = \omega_{c1}^*/2\pi$ , expressed as  $Re_{c1}$  versus  $De/Re$ , obtained from (4.7). The maximum critical frequency for a given  $De/Re$  is denoted by •.

on either side of  $f_{c2}^*$ , say  $f^* = 2$  Hz and  $f^* = 8$  Hz, marked by the vertical arrows in figure 6(b). As illustrated in figure 7(b) (at  $f^* = 2$  Hz), the threshold for stabilization of the monotonic mode,  $\mathcal{A}_s$ , marked by the open circle, has a lower value compared with the critical amplitude for the onset of the oscillatory instability,  $\mathcal{A}_o$ , marked by the filled circle. By contrast, in figure 7(c) (at  $f^* = 8$  Hz), we observe the opposite trend. Thus, there must be a critical frequency at which  $\mathcal{A}_s$  equals  $\mathcal{A}_o$ . Beyond this value, a resonant instability is observed and stabilization of a gravitationally unstable system can no longer be achieved.

Let us first consider how  $f_{c2}^*$  changes with elasticity. Recall from § 3 that the damping rate increases with an increase in  $De$  in the low Deborah number regime ( $De/Re < 1/10$ , cf. figure 2a), whereas it decreases with an increase in  $De$  in the large Deborah number regime. This translates into an increase in  $\mathcal{A}_o$  with increasing  $De$  in the low  $De$  region, therefore shifting  $f_{c2}^*$  to the right and *vice versa* in the large  $De$  region. We illustrate this change within the large  $De$  region using figure 9(a), where all parameters are the same as in figure 6, except for  $De/Re$ , which is now much lower, i.e.  $De/Re = 2/5$ . As a result  $f_{c2}^*$  shifts to the right, and the region where stabilization can be achieved displays several islands of stability, due to the choppiness of the threshold,  $\mathcal{A}_o$ , for the oscillatory mode. However, the bounds for the monotonic and oscillatory modes do not intersect in the low-frequency regime, as predicted by (4.7), which requires  $De/Re > 2/5$  for the existence of  $f_{c1}^*$ . Thus, there is only one critical frequency, i.e.  $f_{c2}^*$ .

Another interesting limit to consider is where the stabilization region in figure 6(b) disappears entirely. This is shown in figure 9(b), where all parameters are the same as in figure 6, except for  $B$ , which is now higher, i.e.  $B = 0.32$ . An increase in Bond number,  $B$ , i.e. an increase in gravitational acceleration, necessitates higher values of forcing amplitudes,  $\mathcal{A}_s$ , for complete stabilization. However, it does not significantly change  $\mathcal{A}_o$ . Consequently, the value of  $f_{c2}^*$  decreases and the region of stability in figure 6(b) shrinks. At a certain Bond number value, the first and the second critical frequencies coincide, i.e.  $f_{c1}^* = f_{c2}^*$ , and stabilization via parametric forcing can no longer be achieved. For the viscoelastic fluid under consideration in figures 6(b) and 9(b), this value is  $B = 0.32$ .

In summary, while moving from figure 6(b) to figures 9(a) and 9(b), we observe either two, one, or zero critical frequencies, i.e. the stabilization region is bounded either on both sides, on one side or is simply non-existent.

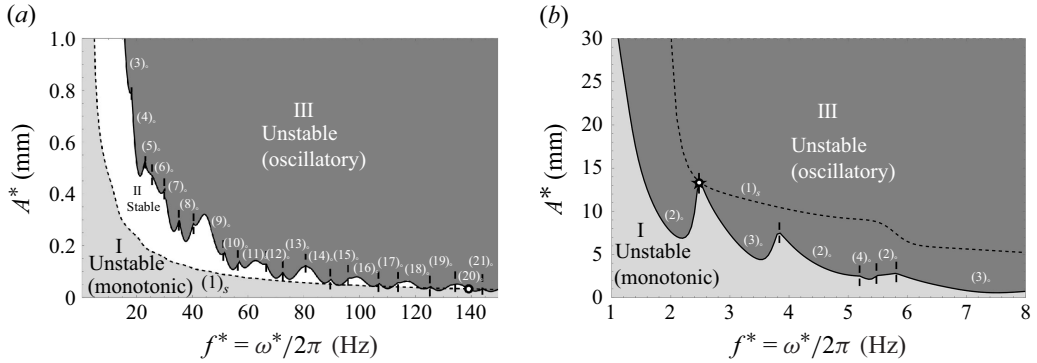


Figure 9. Stability bounds using the same properties as in figure 6 except for different values of  $De/Re$  and  $B$ . (a) Single critical frequency for  $B = 0.1$  and  $De/Re = 2/5$ ; (b) coinciding critical frequencies for  $B = 0.32$  and  $De/Re = 2$ . The  $\star$  marks  $f_{c1}^* = f_{c2}^*$ .

## 6. Summary

In this work, the stability characteristics of a viscoelastic fluid layer undergoing parametric forcing in both gravitationally stable ( $\mathbf{g} > \mathbf{0}$ ) and unstable ( $\mathbf{g} < \mathbf{0}$ ) configurations have been investigated by calculations that are supported by analytical expressions. The inverse time constants,  $\sigma$ , obtained in the absence of forcing for  $\mathbf{g} > \mathbf{0}$  are used to gain insight into the threshold amplitudes and the temporal response of the Faraday instability. In particular, we track how the real part of the leading  $\sigma$ , i.e. the damping rate, changes with elasticity. For weakly elastic fluids, we find that increased elasticity increases the damping rate, thereby raising the Faraday instability threshold. By contrast, for dominantly elastic fluids, the damping rate is reduced with increasing elasticity, thus decreasing the threshold.

The imaginary part of the inverse time constants informs us about the temporal response of the interface to Faraday instability. We find the possibility of both purely real  $\sigma$ , as well as complex  $\sigma$ , thereby introducing the possibility of both monotonic and oscillatory responses upon instability. We show further that the nature of the response upon parametric forcing is highly dependent on the direction and the magnitude of gravitational acceleration,  $\mathbf{g}$ .

If  $\mathbf{g} > \mathbf{0}$ , an oscillatory response is seen upon resonance, when  $|\mathbf{g}|$  is of the order of Earth's gravity. However, at low  $\mathbf{g}$  and in microgravity ( $\mathbf{g} \sim \mathbf{0}$ ), a dominantly monotonic response will arise, if the momentum-induced inertia is weak compared with elastic effects. For a given viscoelastic fluid, this new type of instability is observed until a critical frequency, beyond which the momentum-induced inertia of the fluid dominates, leading to an oscillatory response. By contrast, in Newtonian liquids, an oscillatory instability is observed at all gravity levels.

If  $\mathbf{g} < \mathbf{0}$ , the stabilizing or destabilizing influence provided by parametric forcing changes with the fluid's elasticity. We find that a stable quiescent state is achievable when forced within a finite amplitude range between two critical frequencies. For amplitudes below this range, a monotonic response is observed due to a Rayleigh–Taylor instability mechanism. For amplitudes above this range, an oscillatory response is observed on account of a Faraday instability mechanism. The quiescent stable region disappears if the frequency is either decreased below the first critical frequency or increased beyond the second critical frequency.

The first critical frequency depends on both the fluid's elasticity and viscosity, characterized by  $De/Re$ . The value of the second critical frequency is additionally dependent on the magnitude of the gravitational acceleration,  $\mathbf{g}$ , characterized by the Bond

number,  $B$ . At frequencies below the first critical frequency, parametric forcing promotes monotonic growth of the interface due to the weak influence of fluid inertia. However, at frequencies greater than the second critical frequency, inertia dominates, causing the system to exhibit oscillatory instability before stabilization can be possibly achieved. Consequently, outside the range bounded by the two critical values, the fluid is always unstable, with the system directly transitioning from monotonic to oscillatory instability. The stabilization region is the largest for weakly elastic fluids, for which the first critical frequency goes to zero and the second critical frequency increases significantly due to a higher Faraday threshold. Conversely, for strongly elastic fluids, the stabilization region decreases and then entirely disappears for a large enough Bond number.

Thus, we find for viscoelastic fluids that the number of critical frequencies are two, one or none. This stands in stark contrast with the case of Newtonian fluids, where the region of stabilization is always bounded by a single critical frequency. It might be noted that complete stabilization is possible because the parametric forcing is normal to an erstwhile flat interface in the fluid's base state. On the other hand, if other directions of parametric forcing are considered, the base state will necessarily involve sloshing and a non-flat interface in containers of finite horizontal extent as opposed to unbounded containers, cf. Or (1997). Therefore, complete stabilization to a quiescent state would not be possible in bounded containers with horizontal forcing (Wolf 1969; Shevtsova *et al.* 2016; Garcia-Gonzalez 2017; Gligor *et al.* 2020; Piao & Juel 2025). Notwithstanding a non-trivial base state, future studies ought to consider other directions of parametric forcing due to their interesting physics (Piao & Juel 2025).

The work in this study has used an upper convected Maxwell fluid as an example of a viscoelastic fluid. As there are several examples of Rayleigh–Taylor instability with soft solids (Mora *et al.* 2014; Riccobelli & Ciarletta 2017; Tamim & Bostwick 2020; Dinesh & Narayanan 2021; Slutzky *et al.* 2023), studies on the effect of  $\mathcal{G}$  on parametric forcing of other types of fluids and soft solids could be future avenues of research.

**Funding.** The authors gratefully acknowledge funding from National Science Foundation (R.N., grant numbers 2025117, 2422919) and NASA (R.N., grant numbers NNX17AL27G, 80NSSC23K0457). I.B.I. acknowledges support from a Chateaubriand fellowship.

**Declaration of interests.** The authors report no conflict of interest.

## Appendix A. Derivation of the linear WRIBL model from § 2.3 and the algebraic expressions in table 1 and §§ 4.2 and 4.3.

In this appendix, we derive the linear long-wave model introduced in § 2.3, which is based on the WRIBL (weighted residual integral boundary layer) approach (Ruyer-Quil & Manneville 2000), and which we have used to obtain the algebraic expressions for the inverse time constants in table 1 and the expressions for neutral stability bounds in §§ 4.2 and 4.3.

### Long-wave approximation

We commence by invoking the long-wave approximation, i.e.  $\epsilon \ll 1$ , where  $\epsilon = d^*/W^*$  is the length scale ratio according to the scaling introduced in (2.8). Then, truncating the linearized governing equations (2.17)–(2.23) at  $O(\epsilon)$ , we obtain the continuity equation

$$ku + \frac{\partial w}{\partial z} = 0, \quad (\text{A1})$$



and the momentum equations

$$\epsilon Re\left(\sigma + \frac{i n \omega}{2}\right) u = \epsilon k p + \frac{\partial \tau_{xz}}{\partial z} \quad (\text{A2})$$

and

$$-\epsilon \frac{\partial p}{\partial z} = 0, \quad (\text{A3})$$

where we have assumed  $Re$  to be at least  $O(1)$ . Inertia, which plays an important role in Faraday instability, is retained as it enters at  $O(\epsilon)$  in (A2). Applying the same procedure to the relevant component of the constitutive equations for the polymeric stresses (2.19), we obtain

$$\left(1 + De\left(\sigma + \frac{i n \omega}{2}\right)\right) \tau_{xz} = \frac{\partial u}{\partial z}, \quad (\text{A4})$$

where we have assumed  $De$  to be at least  $O(\epsilon)$ .

The boundary conditions at the bottom wall (2.20),  $z = -1$ , become

$$u = 0 \text{ and } w = 0, \quad (\text{A5})$$

and the interphase coupling conditions, (2.21)–(2.23), at  $z = 0$  become

$$\epsilon w = \epsilon \left(\sigma + \frac{i n \omega}{2}\right) h, \quad (\text{A6a})$$

$$\tau_{xz} = 0, \text{ i.e., } \frac{\partial u}{\partial z} = 0 \quad (\text{A6b})$$

$$\text{and } \sum_{n=-N}^{n=N} e^{(i n \omega t)/2} \epsilon \hat{p}_n = \sum_{n=-N}^{n=N} e^{(i n \omega t)/2} \left\{ \epsilon (\mathcal{G} + \mathcal{A} \cos(\omega t)) \hat{h}_n + \frac{\epsilon^3}{Ca} k^2 \hat{h}_n \right\}, \quad (\text{A6c})$$

where we have assumed  $\mathcal{G}$  and  $\mathcal{A}$  to be at least  $O(1)$  and  $Ca$  to be at least  $O(\epsilon^2)$ . We remind the reader that (A1)–(A6b) imply summation over all the temporal modes introduced in (2.14) and (2.15), which we had omitted in the writing of (2.17)–(2.22), for convenience.

From (A3), we see that  $p$  is independent of  $z$ . Therefore,  $p$  is fully defined by (A6c), which is then substituted into (A2), resulting in

$$\begin{aligned} & \sum_{n=-N}^{n=N} e^{(i n \omega t)/2} \left\{ \epsilon Re\left(\sigma + \frac{i n \omega}{2}\right) \hat{u}_n \right\} \\ &= \sum_{n=-N}^{n=N} e^{(i n \omega t)/2} \left\{ \left[ \frac{\epsilon^3}{Ca} k^3 + \epsilon (\mathcal{G} + \mathcal{A} \cos(\omega t)) k \right] \hat{h}_n + \frac{\partial \hat{\tau}_{xz n}}{\partial z} \right\}. \end{aligned} \quad (\text{A7})$$

Finally, (A7) is inserted into (A4), to obtain

$$\begin{aligned} & \sum_{n=-N}^{n=N} e^{(i n \omega t)/2} \left\{ \left[ 1 + De\left(\sigma + \frac{i n \omega}{2}\right) \right] \left[ \epsilon Re\left(\sigma + \frac{i n \omega}{2}\right) \hat{u}_n \right. \right. \\ & \quad \left. \left. - \frac{\epsilon^3}{Ca} k^3 \hat{h}_n - \epsilon (\mathcal{G} + \mathcal{A} \cos(\omega t)) k \hat{h}_n \right] \right\} = \sum_{n=-N}^{n=N} e^{(i n \omega t)/2} \frac{\partial^2 \hat{u}_n}{\partial z^2}. \end{aligned} \quad (\text{A8})$$



Equation (A8) may be solved for  $\hat{u}_n(z)$  subject to (A5) and (A6b). Inserting this solution into (A1) and integrating the latter from  $z = -1$  to  $z = 0$ , while invoking (A5) and (A6a), yields a characteristic equation for the eigenvalue,  $\sigma$ . This equation may be viewed from two perspectives. In the first perspective,  $\mathcal{A}$  is set to zero, which implies  $N = 0$ , yielding a transcendental algebraic equation for  $\sigma(k^2)$ , which must be solved numerically for the roots. In the second perspective,  $\sigma$  is set to zero and an equation of the form (2.24) is obtained, which must be solved numerically for  $\mathcal{A}$ , yielding the critical forcing amplitude.

However, by applying the WRIBL approach to the linearized equations, (A1) and (A8), an approximate characteristic equation for  $\sigma$  can be obtained, which is analytically tractable in certain limits. This is due to the integral nature of the WRIBL approach, which dispenses with needing to solve for the eigenfunctions,  $\hat{u}_n(z)$ ,  $\hat{w}_n(z)$  and  $\hat{p}_n$ . In particular, we will obtain analytical expressions for (i)  $\sigma$  in terms of  $k$  in the Newtonian limit and  $\mathcal{A} = 0$  and (ii) the critical  $\mathcal{A}$  in terms of  $k$  for a viscoelastic fluid. Capturing the dependency on  $k$ , turns out to be crucial in our current system.

### The WRIBL model

We reduce the dimension of the system of governing equations (A1) and (A8) by eliminating all spatial dependence and describing the flow in terms of the flow rate,  $q$ , and interface deflection,  $h$ . This is achieved by integrating (A1) and (A8) across the film thickness, i.e. from  $z = -1$  to  $z = 0$ . To this end, we integrate the continuity equation (A1) and invoke (A6a). This yields

$$\left(\sigma + \frac{i n \omega}{2}\right) h + k q = 0, \quad (\text{A9})$$

where  $q = \int_{-1}^0 u \, dz$ .

We next obtain an integrated form of the integral momentum equation. To do this we first decompose the dependent variable,  $u$ , into a leading-order contribution (denoted by a tilde) and an  $O(\epsilon)$  correction (denoted by a prime), i.e.

$$u(z) = \underbrace{\tilde{u}(z)}_{O(1)} + \underbrace{u'(z)}_{O(\epsilon)}. \quad (\text{A10})$$

The leading-order velocity,  $\tilde{u}$ , is obtained by truncating (A1)–(A8) at  $O(1)$ , restricting  $Ca$  to be at most of order  $O(\epsilon^3)$ .

The boundary value problem, governing  $\tilde{u}$  is

$$\frac{\partial^2 \tilde{u}}{\partial z^2} = K, \quad \tilde{u}|_{z=-1} = 0, \quad \frac{\partial \tilde{u}}{\partial z} \Big|_{z=0} = 0 \quad \text{and} \quad \int_{-1}^0 \tilde{u} \, dz = q, \quad (\text{A11})$$

where  $K$  is a constant.

Solving (A11), yields

$$\tilde{u} = -\frac{3q(z^2 - 1)}{2}, \quad (\text{A12})$$

which implies for the velocity correction,  $u'$ ,

$$\int_{-1}^0 u' \, dz = 0, \quad u'|_{z=-1} = 0 \quad \text{and} \quad \frac{\partial u'}{\partial z} \Big|_{z=0} = 0. \quad (\text{A13})$$

We next introduce (A10), (A12) and (A13) in (A8), truncate the resulting equations at  $O(\epsilon)$ , multiply by a weight function  $F(z)$  to be determined later, and integrate across the

film height, obtaining

$$\sum_{n=-N}^{n=N} e^{(in\omega t)/2} \left\{ \int_{-1}^0 \left[ 1 + De \left( \sigma + \frac{in\omega}{2} \right) \right] \left[ \epsilon Re \left( \sigma + \frac{in\omega}{2} \right) \widehat{u}_n - \frac{\epsilon^3}{Ca} k^3 \widehat{h}_n - \epsilon (\mathcal{G} + \mathcal{A} \cos(\omega t)) k \widehat{h}_n \right] F \, dz \right\} = \sum_{n=-N}^{n=N} e^{(in\omega t)/2} \boxed{\int_{-1}^0 \frac{\partial^2}{\partial z^2} (\widehat{u}_n + \widehat{u}'_n) F \, dz}, \quad (\text{A14})$$

where the boxed terms in (A14) can be rewritten, upon integration by parts, as

$$\int_{-1}^0 \frac{\partial^2}{\partial z^2} (\widehat{u}_n + \widehat{u}'_n) F \, dz = \left[ \frac{\partial (\widehat{u}_n + \widehat{u}'_n)}{\partial z} F - (\widehat{u}_n + \widehat{u}'_n) \frac{\partial F}{\partial z} \right]_{-1}^0 + \int_{-1}^0 (\widehat{u}_n + \widehat{u}'_n) \, dz. \quad (\text{A15})$$

The weight function,  $F(z)$ , is a polynomial obtained by solving an equation similar to that of the leading-order velocity  $\widehat{u}_n$  (A11). This weighted integration also called the Galerkin projection will cancel all of the  $\widehat{u}'_n$  terms, which are unknown in (A15). The governing equations for  $F$  are

$$\frac{\partial^2 F}{\partial z^2} = 1, \quad F|_{z=-1} = 0 \quad \text{and} \quad \frac{\partial F}{\partial z} \Big|_{z=0} = 0, \quad (\text{A16})$$

yielding

$$F = \frac{1}{2}(z^2 - 1). \quad (\text{A17})$$

This results in the following form of the integrated momentum equation:

$$\sum_{n=-N}^{n=N} e^{(in\omega t)/2} \left\{ \left[ 1 + De \left( \sigma + \frac{in\omega}{2} \right) \right] \left[ \frac{2}{5} \epsilon Re \left( \sigma + \frac{in\omega}{2} \right) \widehat{q}_n - \frac{1}{3} \left( \epsilon (\mathcal{G} + \mathcal{A} \cos(\omega t)) k + \frac{\epsilon^3}{Ca} k^3 \right) \widehat{h}_n \right] + \widehat{q}_n \right\} = 0. \quad (\text{A18})$$

To make the equations applicable when we consider disturbances of arbitrary wavenumbers, we rescale the equations by using a common length scale,  $d^*$ , and time scale,  $d^*/U$ . This results in  $\sigma \rightarrow \sigma/\epsilon$ ,  $\omega \rightarrow \omega/\epsilon$ ,  $k \rightarrow k\epsilon$ ,  $De \rightarrow \epsilon De$ . The resulting equation takes the form

$$\sum_{n=-N}^{n=N} e^{(in\omega t)/2} \left\{ \left[ 1 + De \left( \sigma + \frac{in\omega}{2} \right) \right] \left[ \frac{2}{5} Re \left( \sigma + \frac{in\omega}{2} \right) \widehat{q}_n - \frac{1}{3} \left( (\mathcal{G} + \mathcal{A} \cos(\omega t)) k + \frac{1}{Ca} k^3 \right) \widehat{h}_n \right] + \widehat{q}_n \right\} = 0. \quad (\text{A19})$$

Substituting  $q$  from the integrated continuity equation (A9) into (A19), yields

$$\sum_{n=-N}^{n=N} e^{(in\omega t)/2} \left\{ \left[ 1 + De \left( \sigma + \frac{in\omega}{2} \right) \right] \left[ \frac{2}{5} Re \left( \sigma + \frac{in\omega}{2} \right)^2 + \frac{1}{3} \left( \mathcal{G} k^2 + \frac{1}{Ca} k^4 \right) + \frac{1}{3} \mathcal{A} \cos(\omega t) k^2 \right] \widehat{h}_n + \left( \sigma + \frac{in\omega}{2} \right) \widehat{h}_n \right\} = 0. \quad (\text{A20})$$

which is the same as (2.25).

Characteristic equation for inverse time constant,  $\sigma$

To determine the inverse time constants, we set  $\mathcal{A} = 0$  and  $\omega = 0$  in (A20) and divide the result by  $a$ , yielding a characteristic equation for  $\sigma/a$ , viz.

$$(aDe) \left( \frac{\sigma}{a} \right)^3 + \left( \frac{\sigma}{a} \right)^2 + \left( 1 + \left[ \frac{b}{a} \right] (aDe) \right) \left( \frac{\sigma}{a} \right) + \left[ \frac{b}{a} \right] = 0, \quad (\text{A21})$$

a group that is independent of the characteristic time scale, where  $a = 5/(2Re)$  depends on the viscosity,  $\nu$ , and  $b = (1/3)(k^4/Ca + k^2\mathcal{G})$  depends on the wavenumber,  $k$ . Equation (A21) is the same as (2.26).

Although these  $\sigma$  can be determined numerically from (A21), we shall be interested in the limit  $k \rightarrow 0$ . Algebraic expressions for the  $\sigma$  can then be obtained. This task is enabled by considering the fluid to be of infinite horizontal extent, upon which the unknown dependent variables,  $\psi$ , are now expressed as  $\psi = \psi_0 + \psi_1 e^{ikx} e^{\sigma t}$ , now taking  $k$  to be continuous. This results in the characteristic equation:

$$(aDe) \left( \frac{\sigma}{a} \right)^3 + \left( \frac{\sigma}{a} \right)^2 + \left( \frac{\sigma}{a} \right) = 0. \quad (\text{A22})$$

To obtain these forms,  $\epsilon$  must now be  $d^*/\Lambda^*$  in the scaled forms given in (2.8), where  $\Lambda^*$  is the characteristic wavelength. The cubic equation (A22) yields three roots for  $\sigma$ , with one of the roots being zero. Equation (A22) may be examined in the limit of low  $De$  and high  $De$ .

(i) **Small De.** For small values of  $De$ , a singular perturbation expansion in  $(aDe)$  given by

$$\left( \frac{\sigma}{a} \right) = \frac{1}{(aDe)} \left( \frac{\sigma_{(0)}}{a} \right) + \left( \frac{\sigma_{(1)}}{a} \right) + (aDe) \left( \frac{\sigma_{(2)}}{a} \right) \dots \quad (\text{A23a})$$

is employed to solve (A22). Upon substitution of the expansion, the resulting equations are solved for different powers of  $(aDe)$ . The roots thus obtained are

$$\frac{\sigma_1}{a} = 0, \quad \frac{\sigma_2}{a} = -1 - aDe + O(aDe)^2, \quad \text{and} \quad \frac{\sigma_3}{a} = -\frac{1}{aDe} + 1 + aDe + O(aDe)^2. \quad (\text{A23b})$$

(ii) **Large De.** At large values of  $De$ , since one of the roots is known to be zero, the other two roots can be found from the resulting quadratic equation. The roots obtained using (A22) are

$$\frac{\sigma_1}{a} = 0, \quad \text{and} \quad \frac{\sigma_{2,3}}{a} = -\frac{1}{2aDe} \pm i \sqrt{\frac{1}{aDe} - \frac{1}{4(aDe)^2}}. \quad (\text{A24})$$

These results for the inverse time constants are presented in table 1.

Analytical expression for critical amplitude,  $\mathcal{A}$

The critical amplitude for predicting the onset of monotonic instability due to parametric forcing can be calculated by setting  $\sigma = 0$  and performing the Floquet summation for  $n = -2, 0$  and  $2$ , i.e. thereby considering only the monotonic and lowest harmonic modes. This yields an eigenvalue problem of the form

$$\mathbf{C}\mathbf{x} = \mathcal{A}\mathbf{D}\mathbf{x}, \quad (\text{A25})$$

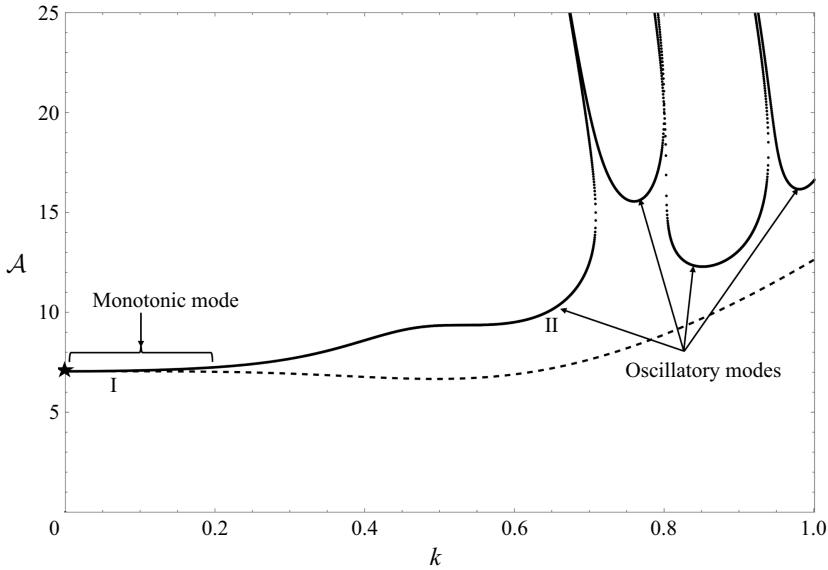


Figure 10. Here  $\mathcal{A}$  versus  $k$  curves. Comparison of threshold obtained using the algebraic expression (A26) (dashed curve) and the numerical results obtained using the full equations (solid curves).

with eigenvalue,  $\mathcal{A}$ , and eigenvectors  $\mathbf{x} = \{\hat{h}_2, \hat{h}_0, \hat{h}_{-2}\}$ . The  $\text{Det}[\mathbf{C} - \mathcal{A}\mathbf{D}]$  must be zero for non-trivial solutions, yielding the square of the critical amplitude as

$$\mathcal{A}^2 = 6 \left( \frac{1}{Ca} + \frac{\mathcal{G}}{k^2} \right) \frac{[(\omega + De\omega c)^2 + c^2]}{(1 + De^2\omega^2)c + De\omega^2}, \quad (\text{A26})$$

where  $c = b - \frac{\omega^2}{a}$ . Note that the frequency is scaled with respect to  $\omega^*$ , the parametric frequency, thereby rendering  $\omega = 1$ . The extent of the monotonic nature of the interface response can be determined from the ratio

$$\frac{\hat{h}_0}{\hat{h}_2 + \hat{h}_{-2}} = \frac{\mathcal{A}}{2 \left( \frac{k^2}{Ca} + \mathcal{G} \right)}. \quad (\text{A27})$$

The algebraic expression (A26), which is the same as (2.28), accurately predicts the critical amplitude at low wavenumbers and when the instability response is monotonically dominant. This is illustrated in figure 10, where this expression, depicted by a dashed curve, is compared with the numerical results obtained using the full-governing equations shown in figure 4(a).

#### Criteria for the existence of a purely monotonic response

We observe from expressions given in (A26) and (A27) that, when  $\mathcal{G} \rightarrow 0$  and  $k \rightarrow 0$ , we have a purely monotonic instability for  $\mathcal{A}^2 \geq 0$ . To see this, we set  $\mathcal{G} = 0$  and  $k = 0$  and determine the parameters for which the expression in (A26) yields a positive value. Equation (A26) becomes

$$\mathcal{A}^2 = \frac{6}{Ca} \frac{[(1 - \frac{De}{a})^2 + (\frac{1}{a})^2]}{[-(1 + De^2)\frac{1}{a} + De]}. \quad (\text{A28})$$

Notice that the numerator in expression (A28) is always positive, thereby requiring the denominator also to be positive. This yields the condition

$$\frac{De}{1 + De^2} > \frac{2Re}{5}. \quad (\text{A29})$$

This criterion for the existence of a pure monotonic instability is presented in § 4.3.

## Appendix B. The detailed form of (2.24) to determine $\mathcal{A}$

The matrix form of the eigenvalue problem in (2.24) is as follows:

$$\underbrace{\begin{bmatrix} C_{N..} & 0 & 0 & 0 & 0 & ..0 \\ 0 & C_{N-1..} & 0 & 0 & ..0 & \\ 0 & 0 & C_{N-2..} & 0 & ..0 & \\ \dots & & & & & \\ 0 & & 0 & ..C_{-N+2} & 0 & 0 \\ 0 & & 0 & 0 & ..C_{-N+1} & 0 \\ 0 & 0 & 0 & 0 & 0 & ..C_{-N} \end{bmatrix}}_{\mathbf{C}} \underbrace{\begin{bmatrix} \hat{h}_N \\ \hat{h}_{N-1} \\ \hat{h}_{N-2} \\ \dots \\ \hat{h}_{-N+2} \\ \hat{h}_{-N+1} \\ \hat{h}_{-N} \end{bmatrix}}_{\mathbf{x}} = \mathcal{A} \underbrace{\begin{bmatrix} 0 & 0 & D_{N-2} & 0.. & 0 & 0 & 0 \\ 0 & 0 & 0 & D_{N-3} & 0.. & 0 & 0 \\ D_N & 0 & 0 & 0 & D_{N-4} & 0.. & 0 \\ \dots & & & & & & \\ 0 & \dots 0 & D_{-N+4} & 0 & 0 & 0 & D_{-N} \\ 0 & 0 & \dots 0 & D_{-N+3} & 0 & 0 & 0 \\ 0 & 0 & 0 & \dots 0 & D_{-N+2} & 0 & 0 \end{bmatrix}}_{\mathbf{D}} \underbrace{\begin{bmatrix} \hat{h}_N \\ \hat{h}_{N-1} \\ \hat{h}_{N-2} \\ \dots \\ \hat{h}_{-N+2} \\ \hat{h}_{-N+1} \\ \hat{h}_{-N} \end{bmatrix}}_{\mathbf{x}} \quad (\text{B1})$$

where  $C_n = (Re(in\omega/2)dc_n/dz - (1/(1 + in\omega De/2)) d^3c_n/dz^3 + (3k^2/(1 + in\omega De/2)) dc_n/dz + \mathcal{G}k^2 + k^4/Ca)|_{z=0}$ ,  $c_n = \hat{w}_n/\hat{h}_n$  and  $D_n = k^2/2$ . Here  $n$  varies from  $-N$  to  $N$ .

## REFERENCES

- ALVES, M.A., OLIVEIRA, P.J. & PINHO, F.T. 2021 Numerical methods for viscoelastic fluid flows. *Annu. Rev. Fluid Mech.* **53** (1), 509–541.
- BALLESTA, P. & MANNEVILLE, S. 2005 Signature of elasticity in the Faraday instability. *Phys. Rev. E* **71** (2), 026308.
- BEVILACQUA, G., SHAO, X., SAYLOR, J.R., BOSTWICK, J.B. & CIARLETTA, P. 2020 Faraday waves in soft elastic solids. *Proc. R. Soc. A* **476** (2241), 20200129.
- BIRD, R.B., ARMSTRONG, R.C. & HASSAGER, O. 1987 Dynamics of polymeric liquids, vol. 1, 2nd edn: *Fluid mechanics*. John Wiley and Sons Inc., New York.
- CABEZA, C. & ROSEN, M. 2007 Complexity in faraday experiment with viscoelastic fluid. *Intl J. Bifurc. Chaos* **17** (05), 1599–1607.
- CHANDRASEKHAR, S. 1961 *Hydrodynamic and Hydromagnetic Stability*. Oxford Clarendon Press.
- DINESH, B., LIVESAY, J., IGNATIUS, I.B. & NARAYANAN, R. 2023 Pattern formation in Faraday instability—experimental validation of theoretical models. *Phil. Trans. R. Soc. A* **381** (2245), 20220081.
- DINESH, B. & NARAYANAN, R. 2021 Branching behaviour of the Rayleigh–Taylor instability in linear viscoelastic fluids. *J. Fluid Mech.* **915**, A63.
- GARCIA-GONZALEZ, S. & FERNANDEZ-FERIA, R. 2017 Stability analysis of the interface between two weak viscoelastic liquids under periodic oscillations. *Phys. Fluids* **29** (1), 013101.
- GLIGOR, D., SÁNCHEZ, P.S., PORTER, J. & SHEVTSOVA, V. 2020 Influence of gravity on the frozen wave instability in immiscible liquids. *Phys. Rev. Fluids* **5** (8), 084001.
- GUYON, E., HULIN, J.P., PETIT, L. & MITESCU, C.D. 2015 *Physical Hydrodynamics*. Oxford University Press.

- IGNATIUS, I.B., DINESH, B., DIETZE, G.F. & NARAYANAN, R. 2024 Influence of parametric forcing on Marangoni instability. *J. Fluid Mech.* **981**, A8.
- KALLIADASIS, S., RUYER-QUIL, C., SCHEID, B. & VELARDE, M.G. 2011 *Falling Liquid Films*. Springer Science & Business Media.
- KUMAR, K. 1996 Linear theory of Faraday instability in viscous liquids. *Proc. R. Soc. Lond. Series A: Math. Phys. Engng Sci.* **452** (1948), 1113–1126.
- KUMAR, K. & TUCKERMAN, L.S. 1994 Parametric instability of the interface between two fluids. *J. Fluid Mech.* **279**, 49–68.
- KUMAR, S. 1999 Parametrically driven surface waves in viscoelastic liquids. *Phys. Fluids* **11** (8), 1970–1981.
- MORA, S., PHOU, T., FROMENTAL, J. & POMEAU, Y. 2014 Gravity driven instability in elastic solid layers. *Phys. Rev. Lett.* **113** (17), 178301.
- MOROZOV, A. & SPAGNOLIE, S.E. 2015 *Introduction to Complex Fluids*. pp. 3–52. Springer New York.
- MÜLLER, H.W. & ZIMMERMANN, W. 1999 Faraday instability in a linear viscoelastic fluid. *Europhys. Lett.* **45** (2), 169–174.
- NAYFEH, A.H. 1981 *Introduction to Perturbation Techniques*. John Wiley & Sons.
- OR, A.C. 1997 Finite-wavelength instability in a horizontal liquid layer on an oscillating plane. *J. Fluid Mech.* **335**, 213–232.
- PIAO, L. & JUEL, A. 2025 Wall-damped Faraday waves in horizontally oscillating two-layer fluid flows. *J. Fluid Mech.* **1002**, R1.
- RAYNAL, F., KUMAR, S. & FAUVE, S. 1999 Faraday instability with a polymer solution. *The Euro. Phys. J. B-Cond. Mat. & Comp. Sys.* **9** (2), 175–178.
- RICCOBELLI, D. & CIARLETTA, P. 2017 Rayleigh–Taylor instability in soft elastic layers. *Phil. Trans. R. Soc. A: Math. Phys. Engng Sci.* **375** (2093), 20160421.
- RUYER-QUIL, C. & MANNEVILLE, P. 2000 Improved modeling of flows down inclined planes. *Eur. Phys. J. B* **15** (2), 357–369.
- SCHÖN, F. & BESTEHORN, M. 2023 Instabilities and pattern formation in viscoelastic fluids. *Eur. Phys. J. Special Topics* **232** (4), 375–383.
- SHAO, X., BEVILACQUA, G., CIARLETTA, P., SAYLOR, J.R. & BOSTWICK, J.B. 2020 Experimental observation of Faraday waves in soft gels. *Phys. Rev. E* **102** (6), 060602.
- SHAO, X., SAYLOR, J.R. & BOSTWICK, J.B. 2018 Extracting the surface tension of soft gels from elastocapillary wave behavior. *Soft Matt.* **14** (36), 7347–7353.
- SHEVTSOVA, V., GAPONENKO, Y.A., YASNOU, V., MIALDUN, A. & NEPOMNYASHCHY, A. 2016 Two-scale wave patterns on a periodically excited miscible liquid–liquid interface. *J. Fluid Mech.* **795**, 409–422.
- SLUTZKY, M., HWANG, J., STONE, H.A. & NUNES, J.K. 2023 Rayleigh–Taylor instability in soft viscoelastic solids. *Langmuir* **40** (2), 1567–1575.
- SOBTI, A., TOOR, A.P. & WANCHOO, R.K. 2018 Oscillatory and steady shear rheological properties of aqueous polyacrylamide solutions. *Chem. Data Coll.* **17–18**, 356–369.
- STERMAN-COHEN, E., BESTEHORN, M. & ORON, A. 2017 Rayleigh–Taylor instability in thin liquid films subjected to harmonic vibration. *Phys. Fluids* **29** (5), 052105.
- SURESHKUMAR, R. & BERIS, A.N. 1995 Effect of artificial stress diffusivity on the stability of numerical calculations and the flow dynamics of time-dependent viscoelastic flows. *J. Non-Newtonian Fluid Mech.* **60** (1), 53–80.
- TAMIM, S.I. & BOSTWICK, J.B. 2020 A dynamic analysis of the Rayleigh–Taylor instability in soft solids. *Extreme Mech. Lett.* **40**, 100940.
- WAGNER, C., MÜLLER, H.W. & KNORR, K. 1999 Faraday waves on a viscoelastic liquid. *Phys. Rev. Lett.* **83** (2), 308–311.
- WOLF, G.H. 1969 The dynamic stabilization of the rayleigh–Taylor instability and the corresponding dynamic equilibrium. *Zeitschrift für Physik A Hadrons and Nuclei* **227** (3), 291–300.